Nanoscale

ROYAL SOCIETY OF CHEMISTRY

PAPER

View Article Online
View Journal | View Issue

Cite this: *Nanoscale*, 2024, **16**, 13580

Copper nitroprusside analogue nanoparticles against melanoma: detailed *in vitro* and *in vivo* investigation†

Sanchita Tripathy, [a,b] Swapnali Londhe, [a,b] Arti Patel, ‡[a] Sudipta Saha, ‡[a,b] Yogesh Chandra [a,b] and Chitta Ranjan Patra *[a,b]

Melanoma is the most invasive and lethal form of skin cancer that arises from the malignant transformation of specialized pigment-producing cell melanocytes. Nanomedicine represents an important prospect to mitigate the difficulties and provide significant benefits to cure melanoma. In the present study, we investigated *in vitro* and *in vivo* therapeutic efficacies of copper nitroprusside analogue nanoparticles (abbreviated as CuNPANP) towards melanoma. Initially, *in vitro* anti-cancer activities of CuNPANP towards melanoma cells (B16F10) were evaluated by several experiments such as [methyl-3H]-thymidine incorporation assay, cell cycle and apoptosis assays using FACS analysis, ROS generation using DCFDA, DHE and DAF2A reagents, internalization of nanoparticles through ICP-OES analysis, co-localization of the nanoparticles using confocal microscopy, JC-1 staining to investigate the mitochondrial membrane potential (MMP) and immunofluorescence studies to analyze the expressions of cytochrome-c, Ki-67, E-cadherin as well as phalloidin staining to analyze the cytoskeletal integrity. Further, the *in vivo* therapeutic effectiveness of the nanoparticles was established towards malignant melanoma by inoculating B16F10 cells in the dorsal right abdomen of C57BL/6J mice. The intraperitoneal administration of CuNPANP inhibited tumor growth and increased the survivability of melanoma mice. The *in vivo* immunofluorescence studies (Ki-67, CD-31, and E-cadherin) and TUNEL assay further support the anti-cancer and apoptosis-inducing potential of CuNPANP, respectively. Finally, various signaling pathways and molecular mechanisms involved in anti-cancer activities were further evaluated by Western blot analysis. The results altogether indicated the potential use of copper-based nanomedicines for the treatment of malignant melanoma.

Received 30th April 2024,
Accepted 14th June 2024

DOI: 10.1039/d4nr01857e

rsc.li/nanoscale

1. Introduction

Melanoma is the most aggressive and deadly form of skin cancer that tends to have more effects on the younger generation and accounts for the majority of skin cancer deaths.[1–4] It arises from the malignant transformation of pigment-producing cell melanocytes, which are neuroectodermal in origin and distributed throughout the body. Due to the wide distribution of these cells, melanoma can ubiquitously occur irrespective of the anatomical location throughout the body.[5] Melanoma is a serious global concern to Caucasian populations as they lack skin pigmentation as compared to dark skinned populations.[6] As per the latest report by the World Health Organization (WHO), there were 3 30 000 new melanoma cases worldwide in 2022 and 60 000 people died from this disease.[7] Moreover, the global melanoma therapeutic market value in 2022 is USD 5.5 billion and expected to increase to USD 14.59 billion by 2032 with an annual growth rate of 10.3%.[8] Moreover, according to an estimate by the American Cancer Society, about 1 00 640 new melanoma cases will be diagnosed in 2024, out of which 8290 people are expected to die from this disease.[9] The conventional treatment strategies for the treatment of melanoma include surgery, chemotherapy, radiotherapy, immunotherapy and targeted therapy.[10] Among them, chemotherapy is the most popular and convenient approach. Unfortunately, the unmet medical challenges with this therapy include non-specificity, resistance to drugs, less effectiveness, toxicity-related issues, limiting long-term therapeutic effects and remission and recurrence of melanoma.[1,2,11] Therefore, new treatment options are urgently needed in order to overcome the difficulties associated with the conventional therapy.

[a]*Department of Applied Biology, CSIR-Indian Institute of Chemical Technology, Uppal Road, Tarnaka, Hyderabad – 500007, Telangana State, India. E-mail: crpatra@iict.res.in, patra.chitta@gmail.com; https://sites.google.com/view/crpatragroup/homehttps://scholar.google.co.in/citations?user=uyaWkGQAAAAJ&hl=en+91-40-27191855*

[b]*Academy of Scientific and Innovative Research (AcSIR), CSIR-HRDC Campus, Kamala Nehru Nagar, Gaziabad 201002, U.P., India*

†Electronic supplementary information (ESI) available. See DOI: https://doi.org/10.1039/d4nr01857e

‡Contributed equally.

In this context, because of unusual fundamental properties of particles in nano-dimension, nanotechnology has been extensively used to solve various biological problems including cancer therapeutics.[11,12] Very recently, metal nanomedicines have been investigated for the treatment of several diseases, especially cancers.[13–18] Among various metals, copper-based nanoparticles have attracted considerable attention in several interdisciplinary (agriculture, industry and environmental applications) and biomedical (anti-bacterial, anti-viral, cancer, wound healing, drug delivery, *etc.*) applications due to their distinct physiochemical characteristics.[13,19–21] Apart from this, copper has been used as a drug supplement to an anti-alcoholism drug, disulfiram (FDA-approved), for treating cancers in clinical trials.[22,23] Therefore, copper (Cu) and Cu-based nanomedicines have gained significant interest in the field of cancer biology as it is least explored even they have possible opportunity.[24] Various investigators including our group all over the world are investigating the anti-cancer properties of copper-based nanomedicines.[13,25–28]

To this, our group investigated the anti-cancer properties of CuNPANP in triple-negative breast cancer.[13] These nanoparticles themselves possess anti-cancer activities without any anti-neoplastic agents. Melanoma arises as a global concern because of the unmet medical challenges associated with conventional therapeutics. Considering these issues, in the present study, the therapeutic efficacy of CuNPANP was investigated towards melanoma through *in vitro* experiments as well as in the *in vivo* melanoma model (C57BL/6J mice). The CuNPANP show significant cytotoxic effects towards B16F10 cells and also inhibit the melanoma growth. Moreover, the plausible mechanistic studies behind the anti-cancer efficacy of the CuNPANP were investigated through various experiments. This new copper-based nanomedicine may overcome the existing limitations for the treatment of melanoma after proper biosafety evaluation.

2. Results and discussion

2.1. Synthesis and characterization of CuNPANP

The detailed synthesis and characterization of CuNPANP have been reported in our recently published paper.[13] In the present study, we again synthesized CuNPANP *via* the interaction of copper sulfate and sodium nitroprusside (SNP) under stirring at room temperature. The newly synthesized CuNPANP were characterized by UV-VIS spectroscopy, XRD, TEM, SEM, XPS, *etc.*, and the results are presented in Fig. 1a–e and ESI Fig. 1a–e.† Initially, the absorption spectrum and corresponding transmittance spectrum of CuNPANP suspension in water were monitored using a UV-VIS spectrophotometer. The results in Fig. 1a reveal that the strong absorption peak of CuNPANP is observed around 250–300 nm with λ_{max} = 275 nm. The strong absorption in this region may be due to the principal types of electronic state transitions probably for transition metal complexes.[29] The XRD patterns of CuNPANP were observed between 10° and 60° (2θ) which strongly reflected the

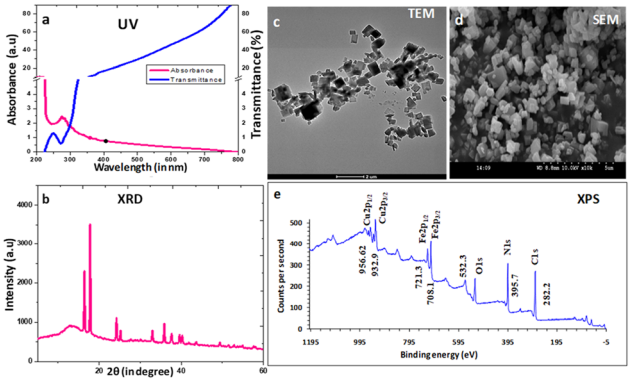

Fig. 1 Characterization of CuNPANP: (a) UV-VIS pattern of CuNPANP, (b) XRD absorption and transmittance spectra of CuNPANP, (c and d) TEM and SEM images of CuNPANP, and (e) XPS survey spectra of CuNPANP.

crystalline nature of nanoparticles, as presented in Fig. 1b. The XRD patterns of CuNPANP were consistent with the published literature including our report.[13,20] Further, the morphologies of the nanomaterials were evaluated through microscopic techniques such as TEM and SEM (Fig. 1c and d). The results revealed that, the particles are cubic in nature with a size ranging between 200 and 500 nm, which corroborates with our earlier published report.[13]

X-ray photoelectron spectroscopy (XPS) analysis was performed to analyze the presence of elements, functional groups and their oxidation state in the CuNPANP.[20,30] Fig. 1e shows the survey spectra of CuNPANP and the corresponding binding energies of the characteristic elements (N 1s, C 1s, O 1s, Cu 2p, Fe 2p) in CuNPANP (Fig. 1e). ESI Fig. 1a–e† present the high-resolution XPS spectra of Cu 2p, Fe 2p, C 1s, N 1s, and O 1s in CuNPANP. The two binding energy values of Cu^{2+} in the CuNPANP observed around 932.9 eV (ref. 31 and 32) and 956.62 eV (ref. 20) may correspond to (Cu^{2+} : Cu $2p_{3/2}$) and (Cu^{2+} : Cu $2p_{1/2}$), respectively (Fig. 1e and ESI Fig. 1a†). The Fe 2p spectra represent the binding energy values at 708.1 eV and 721.3 eV, which correspond to the presence of Fe $2p_{3/2}$ and Fe $2p_{1/2}$ spin orbit components, respectively (Fig. 1e and ESI Fig. 1b†). These peaks originate from the Fe^{2+} species present in the Cu [Fe $(CN)_5$ NO] complex. The high-resolution C 1s spectra of CuNPANP are observed at 282.2 eV, which may be attributed to the C≡N bond present in the nanoparticles (Fig. 1e and ESI Fig. 1c†). The presence of N 1s spectra around 395 eV and 401 eV may be attributed to the presence of CN and NO in the CuNPANP (Fig. 1e and ESI Fig. 1d†). Finally, the O 1 spectra of CuNPANP are observed at 532.3 eV and 528.8 eV, which may be attributed to the O present in the NO group and the adsorbed water molecules in the CuNPANP (Fig. 1e and ESI Fig. 1e†). The XPS data are consistent with the published literature.[20,30]

2.2. Stability studies of CuNPANP

Release or leaching of copper ions from nanoparticles and stability of CuNPANP have been already described in our earlier report.[13] As per the earlier report, the time-dependent

(2 h to 72 h) stability study was carried out by mixing 100 μL of CuNPANP (100 μg) suspension with 900 μL of DMEM or FBS for each time point.[13] The size and charge of the nanomaterials was analyzed using a DLS instrument. The results revealed that there were no significant changes of size and charge over time indicating the stability of the nanomaterials.[13] Furthermore, the stability study of CuNPANP has been carried out in various other buffers or saline including commercially available PBS: C-PBS, freshly prepared phosphate buffer under different pH conditions (P-buffer-pH5.8 and P-buffer-pH7.4) in a time-dependent manner (2 h to 96 h) by analyzing the size and charge of the nanomaterials through a DLS study. The present results also reveal that there is no significant change of size and charge over time, indicating the stability of the materials (ESI Fig. 2a and b†) in buffers or saline over time till 96 h.

As per the earlier report, the release or leaching of copper ions was further examined by centrifugation of the same experimental CuNPANP suspension in DMEM and FBS followed by the collection of supernatant (for each time point) and submission for ICP-OES analysis.[13] The ICP-OES data exhibited the slow release of Cu ions from the nanoparticle (CuNPANP) suspension over time.[13]

It is to be noted here that in general, copper (Cu) exists in two oxidation states (Cu^{1+} and Cu^{2+}). Hence, copper nanoparticles with zero oxidation state or cuprous oxide (Cu_2O) with +1 oxidation state can easily be oxidized to copper oxide (CuO) with +2 oxidation state in the presence of air. In the present study, the CuNPANP or $Cu[Fe(CN)_5NO]$ was synthesized by the interaction of sodium nitroprusside $Na_2[Fe(CN)_5NO]$ and $CuSO_4$, where the oxidation state of Cu is +2 (higher oxidation state). Hence, there is less chance of further oxidation of Cu^{+2} during the drying process using a lyophilized system, as copper is tightly bound to the nitroprusside group. However, the oxidation state of Cu^{+2} in CuNPANP was further confirmed through XPS analysis. Again, CuNPANP do not exhibit any color change in the presence of light or air suggesting no aerial oxidation.

3. Anti-cancer activity of CuNPANP (*in vitro* and *in vivo* approach)

In order to establish the anti-cancer activity of CuNPANP towards melanoma, several *in vitro* and *in vivo* experiments have been conducted, which are discussed in the subsequent sections. The overall scheme for the *in vitro* and *in vivo* anti-cancer studies of CuNPANP towards melanoma is presented in Scheme 1.

3.1. *In vitro* cytotoxic effects of CuNPANP towards B16F10 cells

We have already evaluated and reported the biocompatibility of the CuNPANP through *in vitro* cytotoxicity study in normal cell lines (CHO and HEK) and *ex vivo* hemolysis assay in mouse RBCs.[13] As per the results, the CuNPANP exhibited

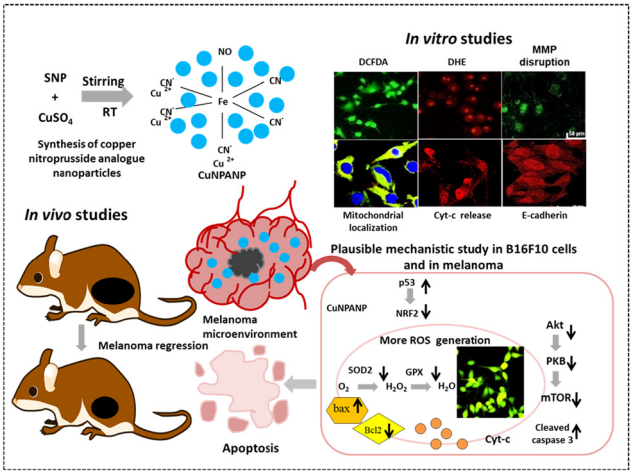

Scheme 1 Overall schematic illustration of the CuNPANP-induced anti-cancer activity through *in vitro* and *in vivo* systems.

minimum or almost no cytotoxicity up to 10 μg mL^{-1} of concentration for 24 h, indicating the biocompatible nature. Moreover, CuNPANP showed no hemolysis up to 20 μg mL^{-1}, which suggests the hemocompatible nature of CuNPANP.[13] Again, the cytotoxic effect of CuNPANP was investigated in various cancer cells (4T1, MDA-MB-231, PANC-1, and B16F10) using MTT reagent.[13] As per the previous report, the dose-dependent (1–20 μg mL^{-1}) cell viability assay in B16F10 cells using CuNPANP showed an IC50 value around 10 μg mL^{-1}.[13] Therefore, in the present study, we conducted all *in vitro* experiments at a concentration of 10 μg mL^{-1}. Furthermore, in the present study, the cytotoxic effect of CuNPANP was evaluated in B16F10 cells through [methyl-3H]-thymidine incorporation assay, as per our earlier report (Fig. 2a).[14] The mouse-specific melanoma cells were incubated with various concentrations of CuNPANP (1–20 μg mL^{-1}) for 24 h. The CuNPANP decrease the B16F10 cell viability in a dose-dependent manner (Fig. 2a). Moreover, the effect of the precursor molecules such as SNP and $CuSO_4$ was evaluated in B16F10 cells through a cellular cytotoxicity assay in a concentration-dependent (1–20 μg mL^{-1}) manner. The precursors ($CuSO_4$ and SNP) are having less inhibitory effects on B16F10 cells up to 20 μg mL^{-1} (Fig. 2b and c) when compared with the CuNPANP treatment (Fig. 2a). These results reveal that the cytotoxic effect of the nanoparticles towards B16F10 cells was mainly observed because of the synergistic activity of precursor molecules.

After evaluating the cytotoxic nature of CuNPANP towards B16F10 cells, the endocytic uptake pathway is investigated through ICPOES analysis (ESI Fig. 3†). To this, the B16F10 cells were pre-incubated with several endocytic pathway inhibitors such as (a) macropinocytosis: amiloride; (b) phagocytosis: Wortmannin; (c) energy-dependent: sodium azide; (d) clathrin-dependent: chlorpromazine hydrochloride; (e) clathrin and caveolae-independent: monensin; (f) caveolae-dependent: methyl-β-cyclodextrin followed by CuNPANP incubation for

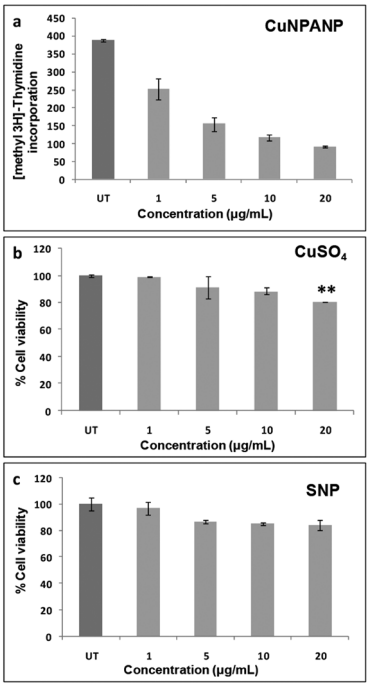

Fig. 2 (a) [Methyl-3H]-thymidine incorporation assay using CuNPANP in B16F10 cells. The CuNPANP decrease the melanoma cancer cell viability in a dose (1–20 μg mL^{-1})-dependent manner. Cell viability assay in B16F10 cells using (b) $CuSO_4$ and (c) SNP in a dose-dependent (1–20 μg mL^{-1}) manner. These experiments were performed thrice and represented as mean ± SD. Significant differences from untreated cells were observed at $^{**}p < 0.01$.

6 h. The internalization of Cu is less when B16F10 cells are pre-incubated with methyl-β-cyclodextrin (0.005 μg of Cu per 10^5 cells) and chlorpromazine hydrochloride (0.011 μg of Cu per 10^5 cells), which are inhibitors of the caveolae- and clathrin-mediated endocytic pathway respectively. However, there is higher accumulation of Cu in B16F10 cells upon incubation with amiloride (0.018 μg of Cu per 10^5 cells), Wortmannin (0.0137 μg of Cu per 10^5 cells), sodium azide (0.0153 μg of Cu per 10^5 cells) and monensin (0.019 μg of Cu per 10^5 cells). Apart from this, the uptake of Cu in B16F10 cells was found to be 0.019 μg per 10^5 cells upon 6 h of incubation. Therefore, we can speculate that, these nanoparticles (CuNPANP) are mainly internalized through caveolae and to some extent through clathrin-mediated endocytosis into the B16F10 cells. The interaction (in the cellular membrane) and trafficking of nanoparticles to the subcellular compartment are essentially important for better therapeutic efficacies.[33]

3.2. Cell cycle and apoptosis analysis

To evaluate the distribution pattern of different phases of cell cycle in B16F10 cells upon CuNPANP incubation, flow cytometry was performed using PI staining as per our published report (ESI Fig. 4a–d†).[13] The results reveal that the nanoparticles arrest B16F10 cells in the G2/M phase and some extent to Sub G1 phase, indicating the apoptosis-inducing potential of CuNPANP as compared to the untreated control cells (ESI Fig. 4a and b†).[34] The cisplatin-treated B16F10 cells are arrested in the G2/M, Sub G1 and S phases (ESI Fig. 4c†) which is supported by earlier report.[35] The corresponding histogram of cell cycle assay is presented in ESI Fig. 4d.†

The cell death inducing property of CuNPANP towards B16F10 cells was evaluated by flow cytometry using Annexin-V FITC with PI staining, as per our published report (ESI Fig. 5a–d†).[13] The results reveal that the CuNPANP induce early and late apoptotic cell death at 18 h time point in B16F10 cells as compared to the untreated cells, as represented in ESI Fig. 5a and b.†[27] The cisplatin-treated B16F10 cells exhibit both late and early apoptotic cell death (ESI Fig. 5c†). The corresponding histogram of apoptosis assay is presented in ESI Fig. 5d.†

3.3. Detection of ROS

To elucidate the plausible mechanisms of apoptosis in B16F10 cells upon CuNPANP treatment, intracellular ROS was determined using DCFDA (H_2O_2, $^{\bullet}NO$, $O_2^{\bullet-}$ and others), DHE ($O_2^{\bullet-}$) and DAF2A (NO) reagents, as per our earlier reports.[13,14,16] These results are presented in Fig. 3a–c^2. The CuNPANP-treated B16F10 cells generate more ROS (H_2O_2, $^{\bullet}NO$, $O_2^{\bullet-}$ and others; more green fluorescence, indicated by white arrow: Fig. $3a^1$) in comparison to the untreated cells (Fig. 3a). TBHP (positive control) treated B16F10 cells accumulate more ROS, as expected (Fig. $3a^2$). The confocal microscopic images were also quantified using the ImageJ software, which is consistent with the above-mentioned observations (ESI Fig. 6a†). Further, the intracellular superoxide ion generation in B16F10 cells upon CuNPANP incubation was evaluated through DHE staining (Fig. 3b–b^2). The CuNPANP accumulate more superoxide anion ($O_2^{\bullet-}$) in B16F10 cells, as indicated by the increased intensity of red fluorescence (Fig. $3b^1$) when compared with the control cells (Fig. 3b). The TBHP-treated B16F10 cells accumulate more $O_2^{\bullet-}$ as expected (Fig. $3b^2$). The corresponding quantification data are presented in ESI Fig. 6b.†

Furthermore, nitric oxide (NO) detection was evaluated in B16F10 cells upon CuNPANP incubation (Fig. 3c–c^2). The confocal microscopic images reveal more nitric oxide generation in the CuNPANP treatment group as marked with increased green fluorescence (Fig. $3c^1$) when compared with the untreated control cells (Fig. 3c). The positive control TBHP induces more NO as expected (Fig. $3c^2$). The quantification data are presented in ESI Fig. 6c.†

3.4. JC-1 staining

There is more ROS accumulation in B16F10 cells upon CuNPANP incubation, which may mediate mitochondrial membrane disruption ($\Delta\Psi_m$) in melanoma cells.[36] Therefore, JC-1 stain is used to investigate the change in $\Delta\Psi_m$ in B16F10 cells and presented in Fig. 4a–c^2. After incubation of CuNPANP in B16F10 cells for 18 h, the relative intensity of red to green fluorescence is increased (as indicated by white arrow; Fig. $4b^1$ and b^2) when compared with the untreated cells (Fig. $4a^1$ and a^2). In the valinomycin-treated B16F10 cells,

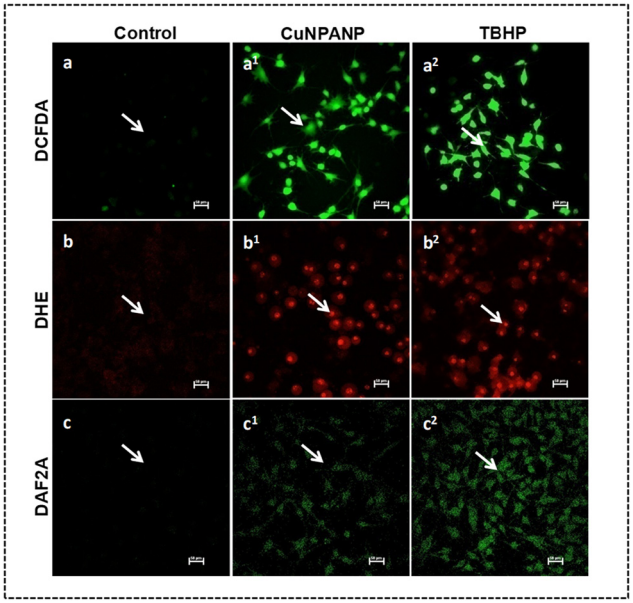

Fig. 3 (a–c^2) Representative images of reactive oxygen species (ROS) detection (indicated by white arrow) in B16F10 cells using (a–a^2) DCFDA, (b–b^2) DHE, and (c–c^2) DAF2A fluorescent dye. Column I: control; II: CuNPANP; III: TBHP. The ROS generation is more (higher green and red fluorescence) in CuNPANP (10 μg mL^{-1})-treated cells (indicated by white arrows) as compared to the untreated control. TBHP is used as the positive control. The images were taken using confocal microscopy (DCFDA: Ex = 480 nm, Em = 535 nm; DHE: Ex = 480–520 nm, Em = 570–600 nm; DAF2A: Ex = 480 nm, Em = 515 nm) at 20× magnification, scale bar = 50 μm.

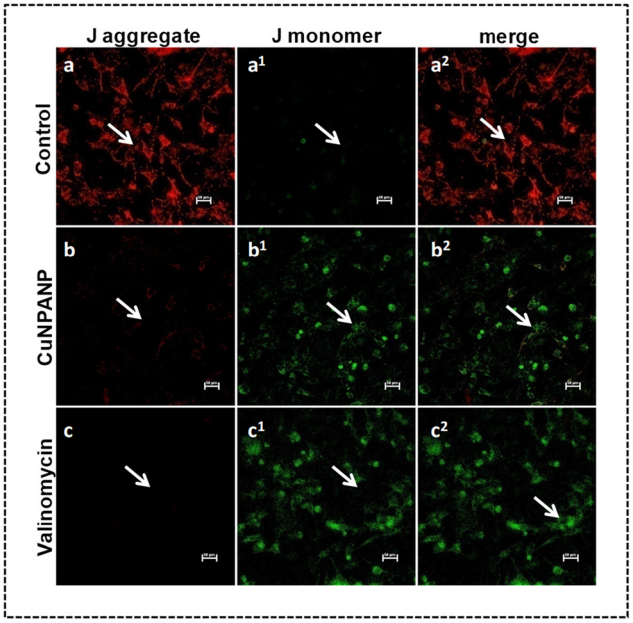

Fig. 4 Representative images of JC-1 staining in B16F10 cells: (a–a^2) control, (b–b^2) CuNPANP, and (c–c^2) valinomycin. Column I: J aggregate; II: J monomer; III: merged images. The CuNPANP-treated groups showed a decrease in mitochondrial membrane potential (JC-1 monomers: indicated by white arrows), as evidenced by the green fluorescence as compared to the untreated control cells (JC-1 aggregate: red fluorescence). Valinomycin is used as positive control. The images were acquired by confocal microscopy (laser: J monomer, λ_{ex} = 520 nm; J aggregate, λ_{em} = 596 nm) at 20× magnification, scale bar = 50 μm.

more intense green fluorescence (as indicated by white arrow) is observed, as expected (Fig. 4c^1 and c^2). The decrease in MMP may be attributed to the amplified oxidative stress in B16F10 cells in response to CuNPANP treatment. This may potentiate apoptotic cell death in B16F10 cells. The confocal microscopic images were quantified using the ImageJ software, and are presented in ESI Fig. 7.†

3.5. Intracellular localization

The intracellular localization of CuNPANP was evaluated in B16F10 cells, as presented in Fig. 5a–d^3. Initially, the B16F10 cells were treated with rhodamine-labeled CuNPANP for 18 h and further incubated with lysotracker and mitotracker green for 15 min in order to stain the lysosome and mitochondria with green fluorescence. The internalized rho-CuNPANP is marked with red fluorescence in the cellular cytoplasm. When the cells are incubated with the rho-CuNPANP followed by incubation with lysotracker green, individual fluorescence was observed in the red and green channels, indicating that the CuNPANP are not localized into the cellular lysosome (Fig. 5c–c^3). However, when the cells are incubated with mitotracker green, yellow fluorescence is observed in the merged images, indicating the co-localization of CuNPANP probably into the cellular mitochondria as presented in Fig. 5d–d^3. Furthermore, no such fluorescence was observed for the untreated (Fig. 5a–a^3) and CuNPANP-treated (Fig. 5b–b^3) as well as rhodamine-incubated (ESI Fig. 8†) B16F10 cells, which further supports the localization of the CuNPANP into the cellular mitochondria.

3.6. CuNPANP amplifies oxidative stress in the cellular mitochondria

The above-mentioned results suggest the internalization of the CuNPANP probably into the cellular mitochondria. Therefore, there is a chance of enhancement of ROS inside the mitochondrial compartment. For this, the mitochondrial ROS accumulation upon CuNPANP incubation was evaluated in B16F10 cells by confocal microscopy using a DCFDA reagent according to earlier published report (Fig. 6a–c).[36] The CuNPANP accumulate ROS inside the B16F10 cells as evidenced by increased green fluorescence (more green fluorescence; indicated by white arrow) (Fig. 6a). The internalized rho-CuNPANP inside the B16F10 cells is marked with red fluorescence (Fig. 6b). In the merged images, patches of yellow fluorescence are distributed throughout the B16F10 cells possibly due to ROS accumulation in the sub cellular organelle mitochondria (Fig. 6c).

3.7. Immunofluorescence studies

The anti-cancer effect of CuNPANP was investigated in B16F10 cells through an immunofluorescence study. Accordingly, the role of cytochrome c (pro apoptotic marker),

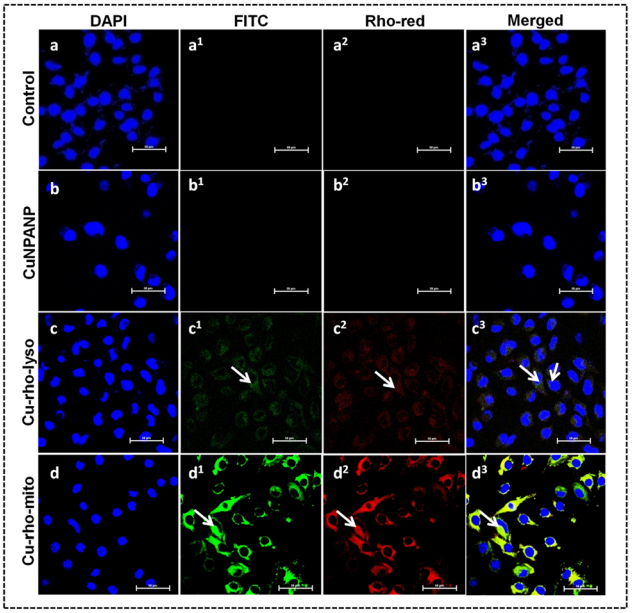

Fig. 5 Representative images of cellular localization of rhodamine-labeled CuNPANP (rho-CuNPANP) in B16F10 cells: (a–a^3) control, (b–b^3) CuNPANP, (c–c^3) Cu-rho-lyso and (d–d^3) Cu-rho-mito. Column I: DAPI; II: FITC: III: Rho-red: IV: merged images. The rho-CuNPANP are localized in the mitochondria, as evidenced by yellow fluorescence (indicated by white arrows). The images were acquired by confocal microscopy (laser used 512 nm and 591 nm for FITC and rho-red channels, respectively) at 60× magnification, scale bar = 50 μm.

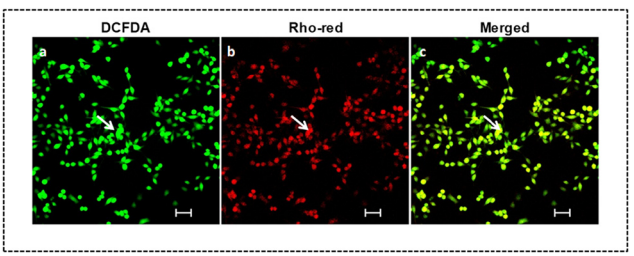

Fig. 6 Representative images of mitochondrial ROS (mito-ROS) generation by rho-CuNPANP in B16F10 cells: (a) DCFDA, (b) rho-red and (c) merged image. The rho-CuNPANP enhances mitochondrial ROS, as evidenced by the yellow fluorescence (indicated by white arrow) in the merged images. The images were acquired by confocal microscopy (laser used 535 nm and 591 nm for FITC and rho-red channel respectively) at 20× magnification, scale bar = 50 μm.

Ki-67 (proliferation marker) and E-cadherin (tumor suppressor gene) was evaluated in response to CuNPANP, and the results are presented in Fig. 7, 8 and 9, respectively. In all the immunofluorescence experiments, cisplatin is used as positive control.

The activation of caspase activators such as cytochrome c is one of the key apoptotic events.[37] Therefore, programmed cell death (apoptosis) inducing properties of CuNPANP were investigated in B16F10 cells through an immunofluorescence study by investigating the expression of cytochrome c. The results

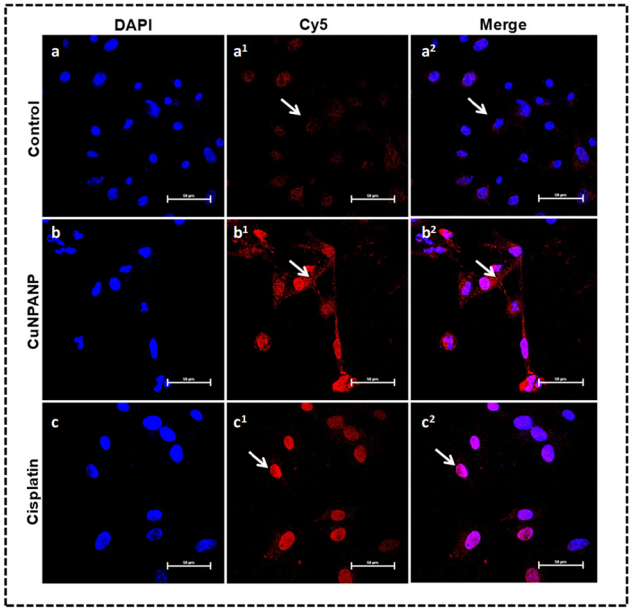

Fig. 7 Representative images of cytochrome c staining in B16F10 cells: (a–a^2) control, (b–b^2) CuNPANP, and (c–c^2) cisplatin. Column I: DAPI; II: Cy5; III: merged images. In the CuNPANP-treated cells, there is increase in the amount of cytochrome c release, as evidenced by the increased red fluorescence (indicated by white arrows) as compared to the untreated control group. Cisplatin is used as the positive control. The images were acquired by confocal microscopy (laser used 488 nm and 594 nm for DAPI and Cy5 channel respectively) at 60 × magnification, scale bar = 50 μm.

are presented in Fig. 7a–c^2. The expression of cytochrome c (indicated with white arrow) is increased in the B16F10 cells upon CuNPANP incubation, which is marked with more red fluorescence and presented in Fig. 7b–b^2, which is mainly attributed to the apoptosis-inducing potential of nanoparticles. However, in the control group, cytochrome c is less expressed (Fig. 7a–a^2). Cisplatin (positive control) shows more cytochrome c release as expected (Fig. 7c–c^2). The corresponding quantification data are presented in ESI Fig. 9.†

Moreover, the expression of Ki-67 was accessed through an immunofluorescence study in B16F10 cells upon CuNPANP incubation (Fig. 8a–c^2). Ki-67 is associated with high-grade melanoma and can be used as a prognostic marker for cutaneous melanoma.[38,39] Therefore, the expression of Ki-67 was investigated in the B16F10 cells. The CuNPANP-treated B16F10 cells are marked with a lower expression of Ki-67, as evidenced by less green fluorescence, which potentiates the anti-cancer properties of the nanoparticles towards melanoma (Fig. 8b–b^2). However, more green fluorescence is observed in the untreated cells due to the proliferative nature of B16F10 cells (Fig. 8a–a^2). There is less expression of Ki-67 in the cisplatin (positive control) treatment group as expected (Fig. 8c–c^2). The corresponding confocal image quantification data are presented in ESI Fig. 10.†

The loss of E-cadherin expression is an important hallmark of melanocytic tumor progression and involved in invasion

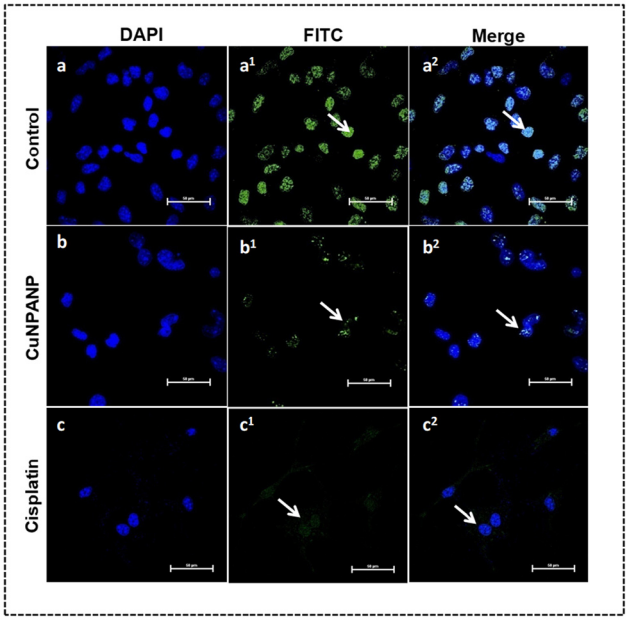

Fig. 8 Representative images of Ki-67 staining in B16F10 cells: (a–a^2) control, (b–b^2) CuNPANP, and (c–c^2) cisplatin. Column I: DAPI; II: FITC; III: merged images. The CuNPANP suppressed the expression of Ki-67 in B16F10 cells, as indicated by less green fluorescence (indicated by white arrows), compared to the untreated control cells (marked by green fluorescence). Cisplatin is used as the positive control. The images were acquired by confocal microscopy (laser used 488 and 535 nm for DAPI and FITC channel respectively) at 60× magnification, scale bar = 50 μm.

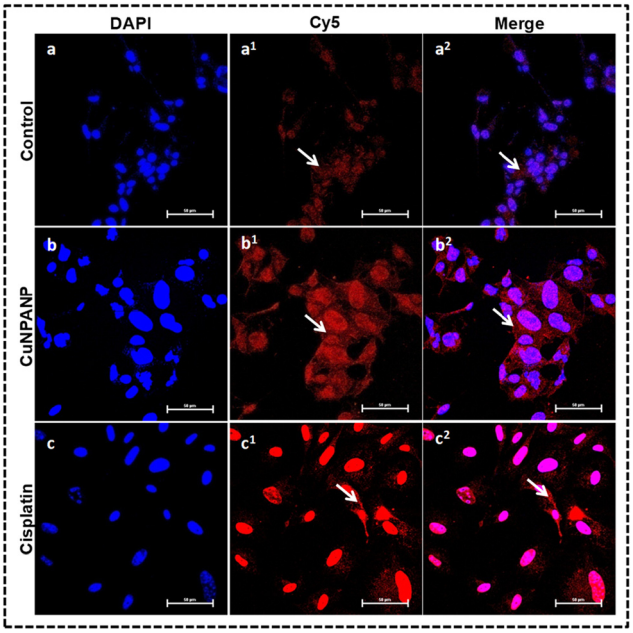

Fig. 9 Representative images of E-cadherin staining in B16F10 cells: (a–a^2) control, (b–b^2) CuNPANP, and (c–c^2) cisplatin. Column I: DAPI; II: Cy5; III: merged images. There is increased expression of E-cadherin in the CuNPANP-treated cells, as evidenced by the increased red fluorescence (indicated by white arrows), compared to the untreated control group. Cisplatin is used as the positive control. The images were acquired by confocal microscopy (laser used 488 and 594 nm for DAPI and Cy5 channel, respectively) at 60× magnification, scale bar = 50 μm.

and metastasis.[40] Therefore, the anti-cancer property of CuNPANP was investigated by analyzing the expression of E-cadherin on B16F10 cells (Fig. 9a–c^2). The expression of E-cadherin is increased in the CuNPANP treatment group (Fig. 9b–b^2), as evidenced by more red fluorescence (indicated by white arrow) when compared with the untreated control cells (Fig. 9a–a^2; suppressed red fluorescence), indicating the anti-cancer nature of CuNPANP. The expression of E-cadherin is increased in the cisplatin-treated cells, as shown in Fig. 9c–c^2. The confocal image quantification results are presented in ESI Fig. 11.†

3.8. Phalloidin staining

The cytoskeletal structure and dynamics in malignant melanoma cells enhance the metastatic potential due to their active participation in cell adhesion, invasion and migration.[41] Therefore, the effect of CuNPANP on the cytoskeletal integrity of B16F10 cells was evaluated through phalloidin staining. The results are presented in Fig. 10a–c^2. In the untreated control group, intact cytoskeletal components are observed (intense green fluorescence) that mainly attributed to the invasiveness of the B16F10 cells (Fig. 10a–a^2). However, in the CuNPANP-treated B16F10 cells, the cytoskeletal network is disrupted, which potentiates the anti-cancer properties of nanoparticles towards melanoma (Fig. 10b–b^2). Cisplatin is used as the positive control, and the expressions of cytoskeletal components are disrupted as expected (Fig. 10c–c^2). The fluorescence quantification of the confocal images is presented in ESI Fig. 12.†

3.9. *In vivo* melanoma regression

In our earlier report, we performed the sighting study of CuNPANP as per OECD guideline no 420, before initiating *in vivo* tumor regression and survivability experiments.[13] Initially, 5 mg kg^{-1} dose of CuNPANP were intraperitoneally administered into the mouse and observed for 2 weeks for any pathological changes. Later, as per the OECD guideline, we used 50 mg kg^{-1} dose of CuNPANP, in which the mouse died. However, at 10 mg kg^{-1} dose, the mouse was healthy and there were no gross pathological changes (such as feed intake, body weight, behavior, along with morbidity and mortality) observed for up to 14 days. As per the sighting study, 10 mg kg^{-1} was the maximum tolerable dose (MTD). Our prior experience of the anti-cancer activity of CuNPANP in breast cancer (sighting study, tumor regression and survivability study) encourages us to perform the anti-cancer activity for melanoma in a pre-clinical mouse model using lower therapeutic doses (1, and -5 mg kg^{-1}).

The *in vitro* anti-cancer properties of CuNPANP in B16F10 cells encouraged us to study the *in vivo* inhibitory potential of the nanoparticles in melanoma. Therefore, we inoculated the mouse-specific B16F10 cells in the lower dorsal right abdomen of a C57BL/6J mouse in order to develop a malignant melanoma model, as per our earlier report.[15] The scheme for

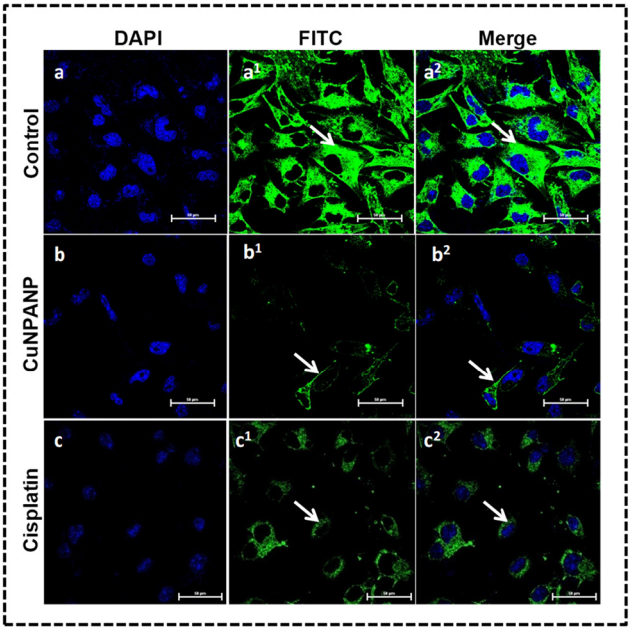

Fig. 10 Representative images of phalloidin staining in B16F10 cells: (a–a^2) control, (b–b^2) CuNPANP, and (c–c^2) cisplatin. Column I: DAPI; II: FITC; III: merged images. The CuNPANP disrupt the cytoskeletal integrity in B16F10 cells, which is marked by decreased green fluorescence (indicated by white arrows) compared to the untreated control cells. The intact cytoskeletal network is observed in the untreated control cells, as evidenced by increased green fluorescence (indicated by white arrows). Cisplatin is used as the positive control. The images were acquired by confocal microscopy (laser used λ_{ex} = 495 nm and λ_{em} = 518 nm) at 60× magnification, scale bar = 50 μm.

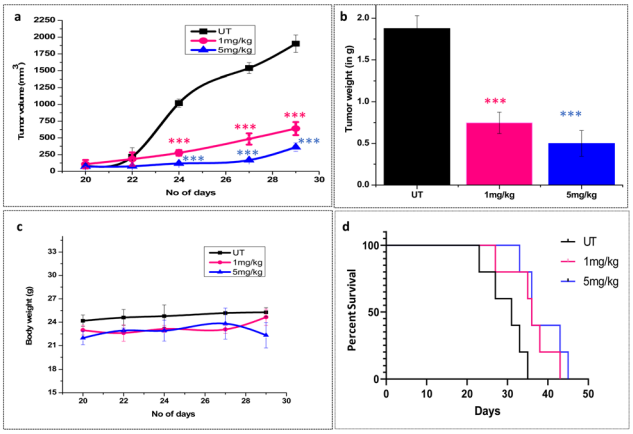

Fig. 11 (a) *In vivo* tumor regression study (n = 5) of CuNPANP in melanoma tumor. The CuNPANP inhibit melanoma tumor growth in different treatment (1- and -5 mg kg^{-1}) groups as compared to the untreated control. (b) Weight of tumor in different CuNPANP (1- and -5 mg kg^{-1})-treated and untreated control groups. (c) Body weight measurement of tumor-bearing mice during the entire study period. (d) Survivability study. The CuNPANP-treated groups (1- and -5 mg kg^{-1}) resulting in 10 days more survival as compared to the untreated control group. These results are presented as mean ± SD. Significant differences from the untreated group were observed at ***p < 0.001.

CuNPANP-mediated malignant melanoma regression and survivability study is represented in Scheme S1.† The melanoma-bearing mice were administered with CuNPANP (1- and -5 mg kg^{-1}) through an intraperitoneal route. The CuNPANP-treated groups inhibit tumor growth when compared with the untreated control group (Fig. 11a). Fig. 11b demonstrates less tumor weight in the CuNPANP treatment group (1- and -5 mg kg^{-1}) compared to the untreated control group, which further potentiates the tumor inhibitory properties of the nanoparticles.

ESI Fig. 13† illustrates the images of tumors and organs in different CuNPANP-treated and control groups that also illustrate the melanoma inhibition potential of CuNPANP towards malignant melanoma. There is no observable body weight change in the tumor-bearing mice in the CuNPANP-treated group (1- and -5 mg kg^{-1}) as compared to the control group during the entire study period, which illustrates the biocompatible feature of the nanoparticles in the *in vivo* system (Fig. 11c) Furthermore, the melanoma inhibitory potential of the nanoparticles was investigated through a survivability study in the malignant melanoma model. The CuNPANP treatment group (1- and -5 mg kg^{-1}) showed more survival (10 days) as compared to the control group (Fig. 11d), which attributes to the tumor inhibitory ability of CuNPANP. Furthermore, the biodistribution of Cu in the tumor and different organs was evaluated through ICPOES analysis and the Cu content was represented as % normalized. The accumulation of Cu is more in the melanoma as compared to the other major organs, as presented in ESI Fig. 14.† The tumor specific uptake of Cu is mainly attributed to the EPR effect, which further supports the therapeutic potential of CuNPANP with fewer side effects.

3.10. Histopathology analysis

To elucidate the changes in response to CuNPANP treatment, H&E staining was performed to investigate the anatomic changes of melanoma tissues and major organs such as liver, kidney, spleen and lungs. In the control group melanoma sections (Fig. 12 column I, Row I), the proliferating neoplastic cells are densely packed with high degree of mitotic figures and there are no necrotic foci in the melanoma stroma. Conversely, in CuNPANP treatment groups (Fig. 12 column I, Row II and III: 1- and -5 mg kg^{-1}), the neoplastic cells exhibit a less compact arrangement, and mitotic figures were significantly reduced. Additionally, there is an increase in multifocal necrotic regions within the tumor mass following CuNPANP treatment. In case of 1 mg kg^{-1}, 50 to 60% of tumor mass consists of necrosis whereas in the 5 mg kg^{-1} group, 70 to 80% of tumor mass consists of necrosis. Furthermore, multifocal inflammatory cell infiltrations are evident in CuNPANP treatment groups (1 mg kg^{-1}: mild degree and 5 mg kg^{-1}: moderate degree).

Major organs were analyzed for any histological changes, but microscopically no abnormalities are found in the liver, kidney, spleen and lungs in the control and CuNPANP-treated groups (1 and -5 mg kg^{-1}). Microscopic examination of the liver specimens from both untreated control and CuNPANP-

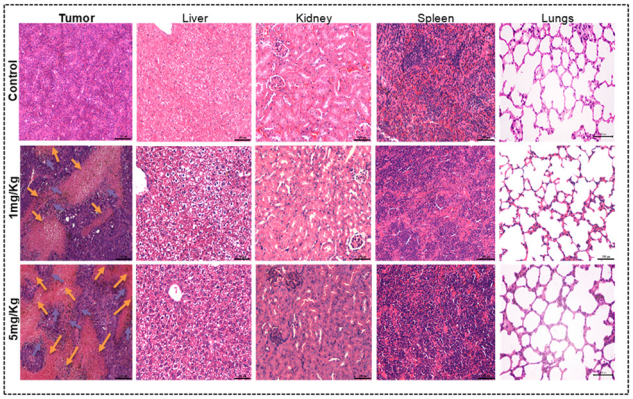

Fig. 12 Representative histopathological images of H&E staining in melanoma and major organs. Column I: melanoma sections; II: liver; III: kidney; IV: spleen; V: lung. Row I: control; II: 1 mg kg^{-1}; III: 5 mg kg^{-1}. The black, green and yellow arrows indicate the presence of mitotic figures, necrotic foci and inflammatory cell infiltrations in the tumor tissue respectively. The images were acquired using a bright field microscope at 20× magnification, scale bar = 100 μM.

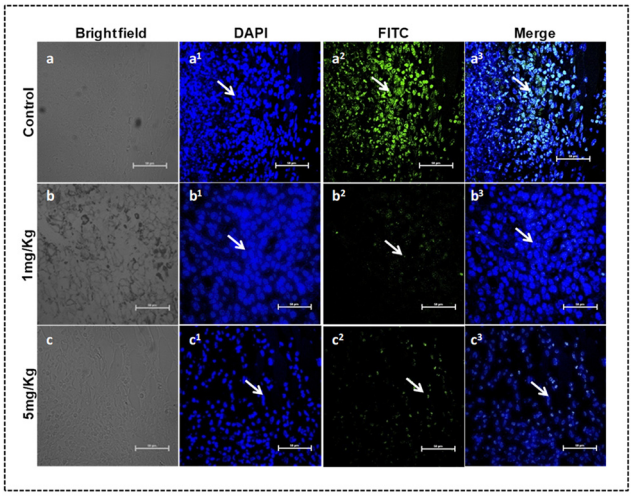

Fig. 13 Representative images of Ki-67 staining in melanoma tumor tissue sections: (a–a^3) control, (b–b^3) 1 mg kg^{-1} and (c–c^3) 5 mg kg^{-1}. Column I: bright field; II: DAPI; III: FITC; IV: merged images. The CuNPANP inhibit the expression of Ki-67 (suppressed green fluorescence as indicated by white arrows) as compared to the untreated control. The images were acquired by confocal microscopy (laser used 488 nm and 535 nm for DAPI and FITC channel respectively) at 60× magnification, scale bar = 50 μm.

treated (1 and -5 mg kg^{-1}) groups revealed distinct hepatocytes characterized by well-defined nuclei and clear sinusoidal architecture, exhibiting a typical and normal morphology of the liver (Fig. 12 column II). Similarly, the kidney sections of control and CuNPANP-treated (1- and -5 mg kg^{-1}) groups showed unaltered tubular structures, intact glomeruli, and unaffected blood vessels, indicative of normal renal morphology (Fig. 12 column III). Furthermore, the examination of spleen samples in the untreated control and CuNPANP-treated groups (1- and -5 mg kg^{-1}) also reveals intact lymphoid follicles, consistent with normal splenic morphology (Fig. 12 column IV). Microscopic examination of lung tissues in the untreated control and CuNPANP-treated (1- and -5 mg kg^{-1}) groups revealed normal alveolar structures devoid of any discernible abnormalities (Fig. 12 column V). These findings collectively indicate the absence of pathological alterations in the organs examined.

3.11. Immunohistochemisty study

The nuclear proliferation marker Ki-67 has clinicopathological significance in malignant melanoma, and is associated with poor prognoses as well as tumor recurrence.[38,39] Therefore, Ki-67 staining was performed in the melanoma tissue sections in order to investigate the tumor inhibitory potential of CuNPANP (Fig. 13a–c^3). There is more intense green fluorescence observed (higher Ki-67 expression) in the control group (UT: column III and Row I) due to the proliferative nature of malignant melanoma (Fig. $13a^2$). However, in the CuNPANP-treated tumor sections (1 mg kg^{-1}: column III and Row II; 5 mg kg^{-1}: column III and Row III) the expression of Ki-67 is decreased as evidenced by less green fluorescence (indicated by white arrow) that supports the tumor inhibitory potential of the nanoparticles towards melanoma (Fig. $13b^2$–c^2). The confocal images were quantified using the ImageJ software, and are presented in ESI Fig. 15,† which match with the *in vitro* immunofluorescence studies, as presented in Fig. 8.

The CD-31/PECAM-1 markers are over expressed in melanoma and involved in the progression of tumors at different morphologic steps.[42] To this, the melanoma inhibitory property of CuNPANP was investigated by evaluating the expression of CD-31/PECAM-1 in the melanoma sections (Fig. 14a–c^3). The expression of CD-31/PECAM-1 is down regulated in the CuNPANP treatment (1 mg kg^{-1}: column III and Row II; 5 mg kg^{-1}: column III and Row III) group, which is marked with less green fluorescence (indicted by white arrows) (Fig. $14b^2$–c^2) as compared to the control group (UT: column III and Row I) (Fig. $14a^2$). The confocal fluorescence images were quantified using the ImageJ software, and are provided in ESI Fig. 16.†

The malignant transformation of melanoma is associated with the loss of E-cadherin expression.[40] Therefore, the expression of E-cadherin was evaluated in the melanoma tissue sections, as presented in Fig. 15a–c^3. The expression of E-cadherin is more (marked with intense green fluorescence) in the CuNPANP-treated tumor tissue sections (1 mg kg^{-1}: column III and Row II; 5 mg kg^{-1}: column III and Row III), which may be attributed to the anti-cancer properties of CuNPANP (Fig. $15b^2$–c^2). However, in the untreated tumor (UT: column III and Row I) sections, the green fluorescence intensity is less (less E-cadherin expression), which may be due to the malignant phenotype of melanoma (Fig. $15a^2$). The fluorescence quantification data are presented in ESI Fig. 17,† which matches with the above-mentioned result and are also

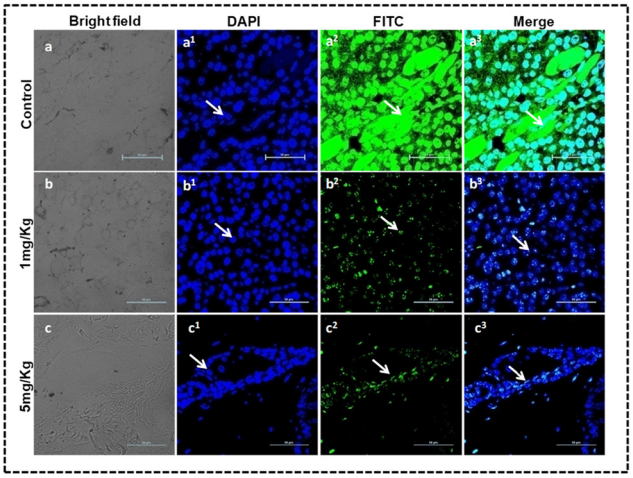

Fig. 14 Representative images of CD31/PECAM-1 analysis in the melanoma tumor tissue sections: (a–a^3) control, (b–b^3) 1 mg kg^{-1} and (c–c^3) 5 mg kg^{-1}. Column I: bright field; II: DAPI; III: FITC; IV: merged images. White arrows indicate suppressed green fluorescence in the treatment group (1, -5 mg kg^{-1}) as compared to the untreated control, suggesting the anti-cancer potential of CuNPANP. All images were acquired by confocal microscopy (laser used 488 nm and 535 nm for DAPI and FITC channel respectively) at 60× magnification, scale bar = 50 μm.

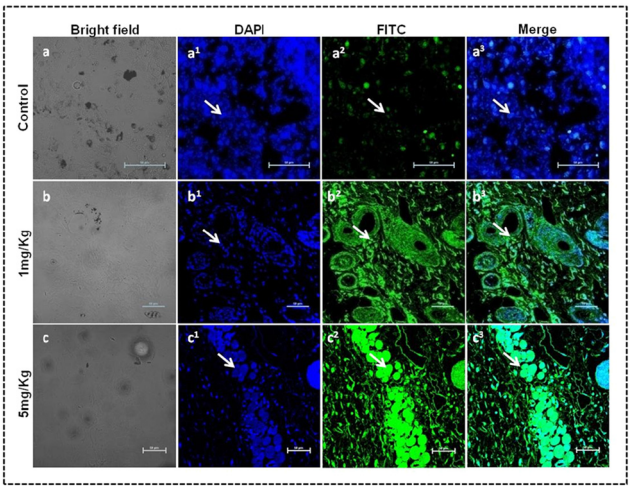

Fig. 15 Representative images of E-cadherin staining in melanoma tumor tissue sections: (a–a^3) control, (b–b^3) 1 mg kg^{-1}, and (c–c^3) 5 mg kg^{-1}. Column I: bright field; II: DAPI; III: FITC; IV: merged images. There is increased expression of E-cadherin (marked by increased green fluorescence) in the CuNPANP-treated (1- and -5 mg kg^{-1}) group as compared to the untreated control. The images were acquired by confocal microscopy (laser used 488 nm and 535 nm for DAPI and FITC channel respectively) at 60× magnification, scale bar = 50 μm.

supported by the *in vitro* immunofluorescence results presented in Fig. 9.

3.12. TUNEL assay

The TUNEL assay was performed in order to investigate the presence of apoptotic region in the melanoma tissue sections

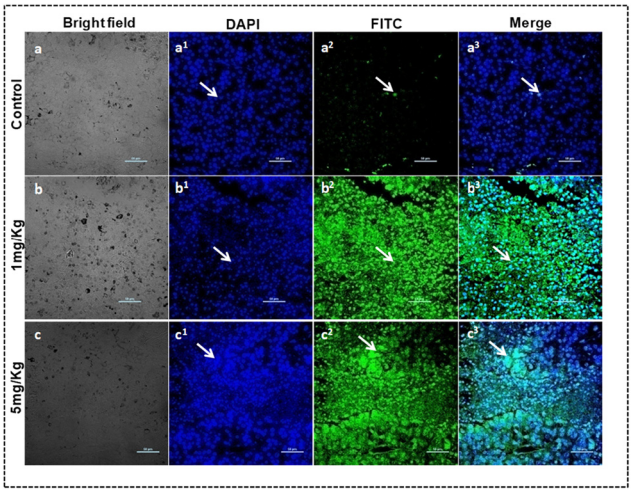

Fig. 16 Representative images of TUNEL assay in the melanoma tumor tissue sections: (a–a^3) control, (b–b^3) 1 mg kg^{-1} and (c–c^3) 5 mg kg^{-1}. Column I: bright field; II: DAPI; III: FITC; IV: merged images. The CuNPANP-treated (1- and -5 mg kg^{-1}) groups showing apoptosis (indicated by white arrows) in the tumor sections as compared to the untreated control. All images were acquired by confocal microscopy (laser used 488 nm and 535 nm for DAPI and FITC channel respectively) at 60× magnification, scale bar = 50 μm.

upon CuNPANP treatment as per our published report (Fig. 16a–c^3).[13] The results reveal that the CuNPANP-treated tumor tissue sections (1 mg kg^{-1}: column III and Row II; 5 mg kg^{-1}: column III and Row III) are marked with increased green fluorescence (Fig. 16b^2–c^2) as compared to the untreated control (UT: column III and Row I) group, as presented in Fig. 16a^2. This is attributed to the presence of apoptotic regions in the melanoma tissue sections, which support the anti-cancer potential of CuNPANP in the malignant melanoma model. The confocal images were quantified using ImageJ, and are presented in ESI Fig. 18.† The results are also consistent with the *in vitro* apoptosis assay, as presented in ESI Fig. 5.†

4. Mechanistic studies through Western blot analysis

Various signaling pathways and molecular mechanisms involved in the melanoma inhibitory potential of CuNPANP towards melanoma were investigated through Western blot analysis in the B16F10 cell and melanoma tissue lysates. For this, the expressions of onco-proteins (Akt, PI3K, mTOR, STAT3, and p53), redox responsive proteins (NRF 2, SOD2, and GPX4) and apoptotic markers (cleaved caspase 3, bax, caspase 3, and Bcl2 cytochrome c) were evaluated in response to CuNPANP exposure (Fig. 17a–c). Based on the published literature, in this study, we hypothesize that the CuNPANP inhibit melanoma growth and progression by inactivating several onco-proteins and redox-responsive proteins as well as by activating the apoptotic pathway, which are presented schemati-

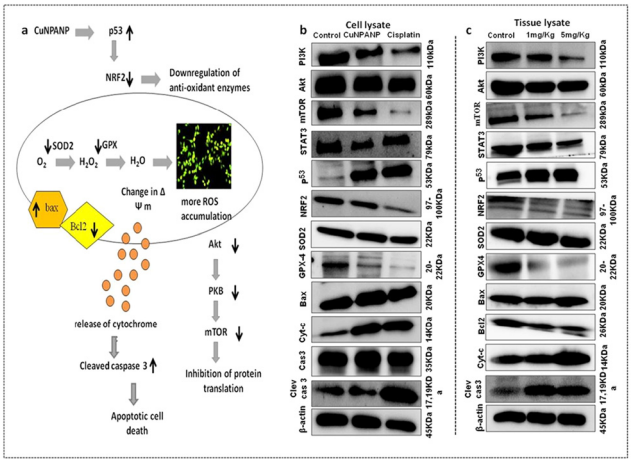

Fig. 17 Western blot analysis of tumor tissue collected from CuNPANP-treated (1- and -5 mg kg^{-1}) and untreated control groups to analyze the expression of PI3K, Akt, m-TOR, STAT3, p53, NRF2, SOD2, GPX4, Bax, cytochrome c, Bcl2, caspase 3, and cleaved caspase 3. β-Actin is used as the loading control. The same source of cell lysate was used to determine the expressions of all proteins in the Western blot experiment.

cally in Fig. 17a.[43–52] Cisplatin was used as the positive control in the *in vitro* Western blot study.

The malignant transformation of melanocytes arises due to genetic alterations, epigenetic dysregulations, metabolic reprogramming and many others.[2,5] There are multiple signaling pathways, which play a pivotal role in the melanoma carcinogenesis. Among the various signaling pathway such as MAPK, JAK-STAT, mammalian target of rapamycin (mTOR), PI3K/Akt signaling involved the growth and progression of melanoma as well as melanoma cell resistance to cytotoxic drugs.[43,44] Therefore, targeting this pathway will provide an important aspect in melanoma. Therefore, the expression patterns of mTOR, PI3K and Akt were examined in the melanoma cell and tissue lysate (Fig. 17b and c). The expressions of these proteins (mTOR, PI3K and Akt) are downregulated in the CuNPANP-treated groups as compared to the untreated control group, which contributes to the melanoma inhibitory properties of CuNPANP through *in vitro* experiments (Fig. 17b) and also in the *in vivo* tumor model (1- and -5 mg kg^{-1}; Fig. 17c). Our results are also consistent with the earlier published report, in which the anti-cancer drug rapamycin (mTOR inhibitor) along with the PI3K and Akt pathway inhibitors sensitizes melanoma cells towards chemotherapy.[53]

Apart from the above-mentioned signaling cascade, the signal transducer and activator of transcription 3 (STAT3) is a major oncogene, which is associated with the progression of melanoma and also emerges as an important target for melanoma treatment.[45] In our study the anti-cancer potential of CuNPANP was investigated by evaluating the expression pattern of STAT3 in the cell and melanoma lysates through Western blot analysis. CuNPANP inhibited the melanoma growth by inactivating the STAT3 expression both in the *in vitro* (Fig. 17b) and *in vivo* (1- and -5 mg kg^{-1}; Fig. 17c) models as compared to the control group.

Other important signaling pathways including p53, NRF2, SOD2, and GPX-4 play a significant role in tumor biology in the context of reactive oxygen species. The ROS acts as a double edge sword, *i.e.* on the one hand, it promotes the growth of tumor cells by activating the mitogenic signaling cascade at lower to moderate concentrations,[46,47,54] and on the other hand, at higher concentrations, it suppresses cell growth through genotoxic stress.[46,47] In the present study, we have already discussed that CuNPANP-treated melanoma cells accumulate more ROS including mitochondrial ROS. The higher amount of ROS probably changes the expression pattern of various signaling proteins such as p53, NRF2, SOD2, and GPX-4 and some of the apoptotic proteins including Bcl-2, cytochrome c, bax, caspase 3 and cleaved caspase 3 in the malignant melanoma cells and tumors. Therefore, we investigated the expression pattern of these proteins to evaluate the anti-cancer properties of CuNPANP towards melanoma.

The interrelation between NRF2 and p53 in the context of ROS has attracted significant attention in cancer biology.[48] In general, these two proteins undergo biphasic modulation under various conditions of ROS. At low to moderate levels, the lower expression of p53 increases the NRF2-dependent antioxidant defense, thereby alleviating ROS and increasing the cell survival. However, at intense oxidative stress, the higher expression of p53 inhibits the anti-oxidant defense through the NRF2-mediated pathway and plausibly helps in the inhibition of tumor growth, which potentiates the tumor suppressor function of p53 through NRF2.[48] Therefore, we have investigated the expression pattern of p53 and NRF2 in the CuNPANP-treated and control groups in both cell and melanoma lysates. The expression of p53 is more in the CuNPANP treatment groups in both *in vitro* (Fig. 17b) and *in vivo* (1- and -5 mg kg^{-1}; Fig. 17c) systems, which contribute to the melanoma inhibitory potential of nanoparticles, as also supported by our earlier report.[55] Further, the expression of NRF2 is less upon CuNPANP treatment as compared to the control group (*in vitro* and *in vivo*), which may increase the anti-cancer properties of nanoparticles towards melanoma through inhibition of the anti-oxidant defense pathway (Fig. 17b and c).[49]

The higher expression of NRF2 in malignant melanoma cells produces intrinsic resistance to anti-cancer therapies and also inhibited ferroptosis-mediated cell death.[51,52] Therefore, targeting or inhibiting the activity of NRF2 in malignant melanoma cells probably induces ferroptosis-mediated cell death by inactivating the activity of GPX-4.[51,52] Moreover, the down regulation of NRF2 also decreases the activity of antioxidant defense enzymes such as glutathione peroxidase (GPXs), superoxide dismutase (SOD) and many others, which probably increases the cancer cell death through accumulation of more ROS.[56] Therefore, we examined the expression pattern of SOD2 and GPX-4 in both cell and tissue lysates of CuNPANP-treated and untreated control groups (Fig. 17b and c). The results reveal that the expression patterns of anti-oxidant protein SOD-2 and GPX-4 are down regulated upon CuNPANP treat-

ment in both *in vitro* and *in vivo* conditions as compared to the untreated control group, thereby probably mediating melanoma inhibition of anti-oxidant defense or mediating ferroptosis (Fig. 17b and c).[50,51]

All these signaling events will converge in order to initiate the apoptotic cell death in melanoma upon CuNPANP incubation.[37] Therefore, we evaluated the expressions of apoptotic markers (Bcl-2, cytochrome c, bax, caspase 3, and cleaved caspase 3) in the cell and tissue lysates of melanoma upon CuNPANP treatment (Fig. 17b and c).[37] The CuNPANP initiate the apoptotic signaling cascade by downregulating the Bcl2 (anti-apoptotic protein) (Fig. 17c) and upregulating bax (pro-apoptotic protein) (Fig. 17b and c), thereby releasing cytochrome c into the cytoplasm in the B16F10 cells and melanoma tissue as compared to the control group (Fig. 17b and c).[13] Furthermore, in order to validate the downstream apoptotic signaling cascade, the expression patterns of caspase-3 and cleaved caspase-3 were evaluated in cell and tissue lysates (Fig. 17b and c). In the CuNPANP treatment group, the expression of caspase 3 (Fig. 17b and c) and cleaved caspase 3 (*in vitro*; Fig. 17b and c) is increased as compared to the control group, exhibiting the apoptosis-inducing nature of CuNPANP towards melanoma.[13] The quantified Western blot data are presented in ESI Fig. 19a and b,† which matched with the above-mentioned results. The original Western blot images of both cell and tissue lysates are provided in ESI Fig. 20a–h.†

5. Overall discussion

Melanoma is the most lethal form of skin cancer that arises from the specialized pigment-producing cells known as melanocytes and also regarded as the fastest growing human cancer, mostly affecting the younger generation.[2,11,57] In recent years, the incidence of melanoma is gradually increasing due to the limited therapeutic options along with the drawbacks associated with the conventional therapeutics especially chemotherapy.[57,58] For this, nanotechnology, especially metal-based nanomedicines, will offer new therapeutic options against melanoma.[57,58] In the current study, the anti-cancer activity of CuNPANP was investigated in detail towards melanoma through various *in vitro* experiments and in the *in vivo* mouse melanoma model along with mechanistic studies.

Initially, the cytotoxic effect of CuNPANP (1–20 μg mL^{-1}) towards B16F10 cells was evaluated through a [methyl-3H]-thymidine incorporation assay, which revealed the dose-dependent cytotoxic effect of the nanoparticles towards the melanoma cell line (Fig. 2a). The precursor ($CuSO_4$, SNP) used for the synthesis of CuNPANP show less inhibitory effects towards melanoma cells, revealing the synergistic properties of both precursors (Fig. 2b and c). After evaluating the cytotoxic effect of CuNPANP, the cellular endocytic uptake pathway study was carried out in B16F10 cells as the interaction and trafficking of nanoparticles are essentially needed for effective anti-cancer therapeutic efficacies.[33] The internalization of the CuNPANP into B16F10 cells is mediated through caveolae- and clathrin-mediated endocytosis (ESI Fig. 3†).[33] Further the anti-cancer properties of the CuNPANP were evaluated through the cell cycle and apoptosis analysis by flow cytometry (ESI Fig. 4 and 5†). The CuNPANP-treated B16F10 cells are arrested in the Sub G1 and G2/M phase (ESI Fig. 4†) and also induce late apoptotic cell death, which is also supported by the earlier published report (ESI Fig. 5†).[13] The *in vitro* plausible mechanistic studies behind the anti-cancer properties of CuNPANP towards B16F10 cells were conducted through ROS (Fig. 3) and immunofluorescence analysis (Fig. 7, 8 and 9). The ROS generation potential of CuNPANP in B16F10 cells was evaluated using different cell permeable fluorescent reagents such as DCFDA (H_2O_2, $^{\bullet}NO$, $O_2^{\bullet-}$ and others), DHE ($O_2^{\bullet-}$) and DAF2A (NO). The CuNPANP-treated B16F10 cells accumulate more ROS (Fig. 3). The more ROS generation eventually disrupt the MMP in the B16F10 cells, which is evaluated through JC-1 staining (Fig. 4).

After investigation of the ROS accumulation potential of the CuNPANP, we were curious to know the sub-cellular localization of the nanomaterials, which was evaluated through confocal microscopy. The rhodamine-conjugated CuNPANP were localized into the cellular mitochondria, which is supported by the yellow fluorescence observed when the cells are incubated with mitotracker green. Moreover, the sub-cellular organelle mitochondria are the major source of cellular ROS. As per our previous observation, the CuNPANP are internalized into the sub-cellular organelle mitochondria, which may help in the accumulation of more ROS in the mitochondria of B16F10 cells that may mediate apoptosis of melanoma cells (Fig. 5). We observed that the CuNPANP-treated B16F10 cells generate mitochondrial ROS as marked by patches of yellow fluorescence in the merged image (indicated by white arrows) (Fig. 6). Furthermore, the anti-cancer properties of CuNPANP were investigated through immunofluorescence studies (cytochrome-c, Ki-67, and E-cadherin) (Fig. 7, 8 and 9). The CuNPANP-treated B16F10 cells induce more cytochrome c release, inhibit Ki-67 expression and also upregulate E-cadherin expression, which altogether supports the anti-cancer properties of the nanoparticles (Fig. 7–9). Furthermore, the CuNPANP disrupt the cytoskeletal integrity of the B16F10 cells, which illustrates the anti-cancer properties of the nanoparticles towards melanoma (Fig. 10).

The *in vivo* studies of CuNPANP were evaluated in the melanoma model through tumor regression and survivability studies, by transplanting B16F10 cells into the dorsal right abdomen of C57BL/6J mice (Fig. 11). The intraperitoneal CuNPANP administration into the melanoma-bearing mice effectively reduce melanoma growth (less tumor volume and weight) as compared to the control group and also enhance the survivability of the melanoma mice (Fig. 11). The CuNPANP are accumulated more in tumors as compared to the other organs in melanoma mice, which may be attributed to the EPR effect (ESI Fig. 14†) Furthermore, the histopathology analysis supports the inhibitory potential of the CuNPANP through the *in vivo* melanoma model (Fig. 12).[5]

Moreover, the various signaling pathways and molecular mechanisms behind the *in vivo* tumor inhibitory properties of the CuNPANP towards melanoma were investigated by performing immunofluorescence studies (Fig. 13–15). The results reveal that the CuNPANP inactivates Ki-67 and CD-31/PFCAM-1 in the melanoma tissue sections. Further, there is increased expression of E-cadherin in CuNPANP-treated melanoma sections. Moreover, CuNPANP treatment increased the apoptotic cell population in the melanoma tissue sections, which further supports the tumor inhibitory properties of the nanoparticles (Fig. 16).

Finally, the mechanism behind the anti-cancer nature of CuNPANP was investigated in the cell and melanoma lysate through Western blot analysis (Fig. 17). The CuNPANP inhibits the expressions of various onco-proteins (Akt, PI3K, mTOR, and STAT3) in the B16F10 cells and melanoma tissues. Moreover, there are increased expressions of p53 in response to CuNPANP, which further inhibit the expressions of NRF2, anti-oxidant protein SOD2, GPX-4 in both B16F10 cells as well as in the melanoma model. These entire signaling cascades finally activate the apoptotic cell death in the melanoma, which is validated by evaluating the expressions of Bcl-2, cytochrome c, bax, caspase 3 and cleaved caspase 3. Altogether, the CuNPANP potentiates the anti-cancer property towards melanoma.

There are numerous reports, in which metal nanoparticles are used as delivery vehicles to carry cancer therapeutic drugs into the tumor microenvironment. In the present study, we did not use any FDA-approved anti-cancer drug as the CuNPANP possess the self-inhibitory potential towards melanoma, which has been briefly elaborated in our recently published report.[13] There are also recent reports, which suggest that iron nitroprusside mediated ferroptotic ovarian cancer cell death *via* GPX-4 inhibition.[59] In this context, the molecular mechanism and signaling cascade behind the anti-cancer properties of CuNPANP were investigated through Western blot analysis. During this study, we observed the downregulation of GPX-4 protein in both B16F10 cells and melanoma tissue upon CuNPANP treatment. We can speculate that the CuNPANP is involved in ferroptosis through inhibition of GPX-4. However, the exact mechanism needs a more in-depth study, which is beyond the scope of our present study.

6. Conclusions

The present work offers a detailed study of the anti-cancer activities of CuNPANP towards melanoma through *in vitro* experiments and their validation in the *in vivo* melanoma model. The *in vitro* studies reveal the cytotoxic nature of CuNPANP towards B16F10 cells and these nanoparticles internalized into the melanoma cells through caveolae- and clathrin-mediated endocytosis as well as localized in the sub-cellular organelle mitochondria. These nanoparticles accumulate more ROS (H_2O_2, $^{\bullet}NO$, $O_2^{\bullet-}$ and others; including mitochondrial ROS) in the melanoma cells that eventually disrupt the MMP, release cytochrome c, inactivate proliferation marker Ki-67, upregulate E-cadherin and also disrupt the cytoskeletal integrity in the B16F10 cells. Furthermore, the CuNPANP inhibit the melanoma growth and increase the survivability of the melanoma-bearing mice in the *in vivo* tumor model. The plausible molecular mechanism and signaling pathways behind the tumor inhibition potential of CuNPANP include the inactivation of Ki-67 and CD-31, upregulation of E-cadherin, suppressed expression of several onco proteins such as PI3K, Akt, and m-TOR as well as downregulation of NRF2, GPX-4, and SOD2, activation of apoptotic signaling proteins and DNA fragmentation. Altogether, our results indicated that the CuNPANP will provide promising therapeutic efficacy towards melanoma.

7. Experimental procedures

7.1. Materials and methods

7.1.1. Chemicals. Sodium nitroprusside (Na_2 [$Fe(CN)_5NO$]), copper sulfate ($CuSO_4 \cdot 5H_2O$), sodium azide, chlorpromazine, Wortmannin, methyl-β-cyclodextrin, 3-(4,5-dimethylthiazol-2-yl)-2,5-diphenyltetrazolium bromide (MTT) reagent, 2′,7′-dichlorodihydrofluorescein diacetate (DCFDA), 4,5-Diaminofluorescein Diacetate (DAF-2DA), dihydroethidium (DHE), ribonuclease (RNase), bovine serum albumin (BSA), propidium iodide, cisplatin, rhodamine B, RIPA buffer, PVDF membrane, TBHP (*tert*-butyl hydroperoxide), Dulbecco's phosphate buffered saline (DPBS), fluoroshield DAPI and methanol were purchased from Sigma Aldrich chemicals, USA. Dulbecco's modified Eagle's medium (DMEM), fetal bovine serum (FBS), acrylamide, bis-acrylamide, trypsin, streptomycin and penicillin were obtained from Himedia. Triton X and Bradford reagent were purchased from Genetix Biotech Asia Pvt. Ltd. Monensin and amiloride were obtained from Alfa-Aesar, Ward Hill, Massachusetts, USA. Dimethyl sulfoxide (DMSO) was obtained from Rankem (India). Mitotracker green and Lysotracker green were purchased from Thermo Fischer Scientific, Grand Island, New York. [Methyl-3H]-thymidine was procured from PerkinElmer Life and Analytical Sciences, Massachusetts, USA.

7.1.2. Antibodies. Primary antibodies: anti-Bcl2 Rabbit mAb (#3498), anti-caspase 3 Rabbit mAb (#9662), anti-STAT 3 Mouse mAb (#83541), anti-cytochrome c Rabbit mAb (#11940), anti-E-cadherin Mouse mAb (#14472), anti-GPX4 Rabbit mAb (#52455), anti-NRF-2 Rabbit mAb (#12721), anti-SOD-2 Rabbit mAb (# 13141), anti-Bax Rabbit mAb(#2772), anti-cytochrome c Rabbit mAb (#11940), anti-cleaved caspase 3 Rabbit mAb (#9664), anti-p53 Mouse mAb (#2524), anti-Akt Rabbit mAb (#4691), anti-PI3K Rabbit mAb (#4249), anti-m-TOR Rabbit mAb (#2983), anti-β-actin Rabbit mAb (#4970), anti-Ki-67 Rabbit mAb (#9129), anti-CD31/PECAM-1 Mouse mAb (#3528), corresponding secondary antibodies: anti-mouse IgG (HRP) (#7076) and anti-rabbit IgG (HRP) (#7074) were purchased from Cell Signaling Technologies Danvers, Massachusetts, USA. Goat anti-

rabbit IgG [H + L] Alexa Flour 488/594 and protein ladder were purchased from Puregene. An ECL Western blotting substrate was obtained from BIO-RAD, Berkeley, California.

7.1.3. Kits. A TUNEL assay kit and a JC-1 mitochondrial staining kit were purchased from Sigma Aldrich, Burlington, Massachusetts, USA. A Nitrate/Nitrite Colorimetric Assay Kit and an Annexin V-FITC with PI Apoptosis Detection kit were acquired from Cayman, Ann Arbor, Michigan, USA. Alexa Fluor® 488 Phalloidin (#8878) was purchased from Cell Signaling Technologies Danvers, Massachusetts, USA.

7.1.4. Cell lines. Mouse-specific melanoma cell line (B16F10) was procured from ATCC.

7.1.5. Animal experiments. All the animal experiments were carried out in C57BL/6J mice (female: 5–8 weeks old) with the approval of the institutional animal ethics committee of CSIR-IICT (Approval no; IICT-IAEC-078 dated 29-12-2021).

7.2. Synthesis and characterization of CuNPANP

The CuNPANP were synthesized according to our published report.[13] For this, one mole each of sodium nitroprusside (SNP) and copper sulfate ($CuSO_4$) were interacted at room temperature under stirring conditions to form CuNPANP. The detailed synthesis procedure of CuNPANP, and their *in vitro* and *in vivo* experiments are elaborately provided in the ESI.†

7.2.1. Nanoparticle suspension. A fresh stock solution of CuNPANP (concentration: 1 mg mL^{-1}) was prepared by mixing 1 mg of CuNPANP in 1 mL of autoclaved MilliQ water. The freshly prepared nanoparticle suspension was sterilized each time under UV irradiation for 20 min before performing the *in vitro* cell culture experiments.

7.2.2. Characterization of CuNPANP. The detailed procedures for the characterization of newly synthesized CuNPANP are elaborately described in the ESI.†

7.2.3. Synthesis of rhodamine-conjugated copper nitroprusside nanoparticles (rho-CuNPANP). Initially, 5 mL of SNP solution (10^{-1} M) was taken in a 50 mL beaker and kept over a magnetic stirrer to which 5 mL of $CuSO_4$ solution (10^{-1} M) was added dropwise under stirring conditions at room temperature. The brown color of the aqueous SNP solution turned into green color instantly. Then, immediately 100 μL of rhodamine suspension (1 μg mL^{-1}) was added into the reaction mixture and stirred for another 2 h. The particles were allowed to settle down and the supernatant was discarded. The solution was washed several times to remove the un-reacted reactants or unbound rhodamine. Finally, a pellet was obtained and dried in a hot air oven (~65 °C) to obtain powdered rho-CuNPANP, which were used for cell culture experiments.

7.3. *In vitro* assays

The mouse-specific melanoma cells (B16F10) were cultured in DMEM supplemented with 1% antibiotic–anti-mycotic solution and 10% FBS and maintained in a humidified incubator under appropriate conditions (5% CO_2, 37 °C).

7.3.1. [Methyl-3H]-thymidine incorporation assay. The [methyl-3H]-thymidine incorporation assay is a gold standard method to evaluate the inhibitory potential of anti-cancer drugs.[60] For this, the inhibitory effect of CuNPANP on B16F10 cells was evaluated by performing a [methyl-3H]-thymidine incorporation assay according to our earlier report.[14] Briefly, B16F10 cells were seeded at a density of 40×10^3 cells per well in a 24-well plate under appropriate conditions. After 24 h, the B16F10 cells are incubated with different concentrations of CuNPANP (1–20 μg mL^{-1}) for 24 h. Then, the cells were incubated with DMEM containing [methyl-3H]-thymidine (1 μC) for 4 h. Following incubation, the cells were washed with PBS and incubated with 0.1% SDS (100 μL) for 1 h for cell lysis. Then, the cells were scrapped and transferred into a 96-well plate followed by the addition of scintillating oil (1 : 1). The radioactivity was measured as counts per minute using a PerkinElmer MicroBeta2 system in a scintillation chamber.

7.3.2. Cellular cytotoxicity assay. The cellular cytotoxic assay was performed with B16F10 cells using the precursor chemicals SNP and $CuSO_4$ in a concentration-dependent manner (1–20 μg mL^{-1}) according to our previous reports[13,16] (for detailed procedure, see ESI†).

7.3.3. Cell cycle assay. To evaluate the distribution of cell cycle phases in the B16F10 cells upon CuNPANP (10 μg mL^{-1}) incubation, flow cytometry was performed according to our earlier report[16] (for detailed procedure, see ESI†).

7.3.4. Apoptosis assay. The apoptotic cell population of B16F10 cells upon CuNPANP (10 μg mL^{-1}) treatment was analyzed using Annexin-V FITC with PI staining according to our published report[15] (for detailed procedure, see ESI†).

7.3.5. Detection of ROS. The effect of CuNPANP on intracellular ROS accumulation was investigated in B16F10 cells using H_2DCFDA, DHE and DAF-2A reagents according to our earlier report.[14] For this, the B16F10 cells were incubated with CuNPANP (10 μg mL^{-1}) for 18 h. Then, the B16F10 cells were incubated with DCFDA (10 μM), DHE (10 μM) and DAF-2A (10 μM) reagents for 35 min and observed using a confocal microscope at 20× magnification (for detailed procedure, see ESI†).

7.3.6. Mitochondrial JC-1 staining. JC-1 stain was used to investigate the changes in the mitochondrial membrane potential (MMP denoted by ΔΨm) upon CuNPANP incubation according to our published reports.[13,36] For this, the B16F10 cells were incubated with CuNPANP for 18 h and processed with JC-1 stain to observe the changes in $\Delta\Psi_m$ in the mitochondria (for detailed procedure, see ESI†).

7.3.7. Cellular localization using a confocal microscope. The intracellular localization of CuNPANP in B16F10 cells was evaluated by confocal microscopy as per published report.[36] Briefly, 1×10^5 cells per well were seeded onto coverslips in a 6-well cell culture plate. On the next day, B16F10 cells were treated with rhodamine-conjugated CuNPANP (rho : CuNPANP : 1 : 100 μL; 5 μg mL^{-1}) for 18 h. The cells were incubated with lyso- and mito tracker green for 15 min just before the termination of rho-CuNPANP incubation. Following a PBS wash, the cells were mounted with fluoroshield DAPI for nuclear staining and examined at 60× magnification using a Nikon TiEclipse Confocal microscope.

7.3.8. Mitochondrial ROS detection. The mitochondrial ROS accumulation in B16F10 cells was investigated by incubat-

ing the cells with rho-CuNPANP and DCFDA according to the earlier report.[36] Briefly, the B16F10 cells (8×10^3 cells per well) were seeded in a 96-well plate at 37 °C in an atmosphere containing 5% CO_2 under appropriate cell culture conditions. After the cells reached 70–80% confluence, they were treated with 5 μg mL^{-1} of rho-CuNPANP for 18 hours. Then, the cells were incubated with DCFDA reagent (10 μM) for 30 min and confocal microscopic images were acquired at 20× magnification using a Nikon Eclipse confocal microscope (TE2000-E, laser used 535 nm and 591 nm for FITC and rho-red channel respectively).

7.3.9. Immunocytochemistry analysis. The anti-cancer nature of CuNPANP was analyzed in B16F10 cells through immunofluorescence (cytochrome-c, Ki-67, and E-cadherin) studies as per our published report.[14] For this, the B16F10 cells were incubated with the nanoparticles (10 μg mL^{-1}) for 18 h and processed with primary (cytochrome-c, Ki-67, and E-cadherin) and secondary (Alexa Fluor 488 and 594) antibodies as well as mounted with fluoroshield DAPI to observe under a confocal microscope at 60× magnification (for detailed procedure, see ESI†).

7.3.10. Cytoskeletal staining. To determine the effect of CuNPANP on the cytoskeletal integrity of B16F10 cells, phalloidin staining was performed as reported in the literature.[61] Briefly, 1×10^5 cells per well were seeded on a coverslip in a 6-well cell culture plate. On the next day, the cells were incubated with CuNPANP (10 μg mL^{-1}) and cisplatin (positive control) for 18 h. The cells were washed with PBS (2 times) and fixed with 4% paraformaldehyde (10 min). After this, the cells were washed with PBS (2 times) and permeabilized for 5 min with 0.2% Triton X. Then, the cells were washed with PBS (2 times) and blocked with 3% BSA for 1 h. Following PBS (2 times) washing, the cells were incubated with Alexa flour 488 phalloidin antibodies (5 μL) for 20 min. After this, the slides were washed 2 times with PBS and mounted with fluoroshield DAPI. The confocal microscopic images were acquired at 60× magnification using a Nikon TiEclipse Confocal microscope (laser used λ_{ex} = 495 nm; λ_{em} = 518 nm).

7.4. *In vivo* anti-cancer study in a melanoma mouse model

For the melanoma regression and survival study, female C57BL/6J mice (5–8 weeks old) were procured from CSIR-IICT Animal House Facility. This study was performed with permission from the institutional animal ethics committee of CSIR-IICT (Approval no; IICT-IAEC-078 dated 29-12-2021).

7.4.1. Experimental design. The *in vivo* melanoma regression and survival study was conducted by inoculating B16F10 cells (2.5×10^5 cells in 100 μL of 1× HBSS buffer) in the dorsal right abdomen of C57BL/6J mice according to our earlier report.[15] Upon reaching a tumor volume of 100–200 mm^3, the melanoma mice were randomly divided into several groups, namely, Group-I: Control/Untreated, Group-II: 1 mg kg^{-1}, and Group-III: 5 mg kg^{-1} in order to investigate the tumor inhibition and survival potential of CuNPANP. The CuNPANP (1- and -5 mg kg^{-1}) treatments were intraperitoneally administered into the melanoma bearing mice for five alternative days (total five doses; over a period of 10 days). The anti-tumor efficacy of CuNPANP against melanoma was evaluated by measuring the tumor volume using formula $V = 0.5 \times (a \times b^2)$ (V is the tumor volume, a is the major diameter, and b is the minor diameter) at different time periods. The mice were carefully observed for clinical symptoms such as loss/gain of body weight, mortality and morbidity throughout the experimental period. In the melanoma regression group, all mice were euthanatized after completion of the nanoparticle treatment and the samples (tumors and other organs) were further analyzed using various assays in order to investigate the anti-cancer property of CuNPANP in the *in vivo* melanoma model. However, in the survivability group, the mice were kept as such after completion of the CuNPANP treatment.

7.4.2. Analysis of tumor inhibition using various assays. After completion of the tumor regression study, tumor samples were collected from different control and CuNPANP-treated (1 and -5 mg kg^{-1}) groups and analyzed for Western blot analysis, immunohistochemical staining (Ki-67, CD-31, and E-cadherin) and TUNEL assays. Further, histological examination was also performed in tumor and major organs (liver, kidney, spleen, and lung) of mice to evaluate the therapeutic efficacy of CuNPANP in melanoma.

7.4.3. Biodistribution of Cu in tumors and different organs. The biodistribution of Cu in tumors and vital organs of melanoma-bearing mice was analyzed through ICPOES analysis, as per our published report.[16] For this, the melanoma samples and organs were harvested with PBS after euthanizing the mice and kept at −80 °C. The samples were weighed and digested with 5 mL of 70% nitric acid and placed in a water bath for 1 h. The digested samples were filtered using a syringe filter and submitted for ICPOES analysis.

7.4.4. Histological analysis. In order to identify the pathological changes in the histological sections of melanoma and major organs of melanoma-bearing mice, H&E staining was performed as per our published report.[13] For this, the tumor samples and major organs (lung, liver, kidney, and spleen) were collected from control and different CuNPANP treatment (1 and -5 mg kg^{-1}) groups after sacrificing the mice. Then, the tissues were fixed (4% *para*-formaldehyde), processed and then incorporated into paraffin blocks. Further, tissue sections (5 μm) were mounted on glass slides and processed for H&E staining. The histopathological appearances of melanoma and major organs were observed using a bright-field microscope at 40× magnification and analyzed by a certified pathologist from random fields in order to provide an unbiased opinion.

7.4.5. Immunohistochemical analysis. The inhibitory potential of CuNPANP was investigated in the melanoma tissue through immunofluorescence studies according to our published report.[13] For immunofluorescence studies, the tumor tissue sections were processed with primary (anti-Ki-67, anti-CD31/PECAM-1, and anti-E-cadherin) and secondary (Alexa Fluor 488) antibodies. The confocal microscopic images were acquired at 60× magnification using a Nikon Eclipse confocal microscope (for detailed procedure, see ESI†).

7.4.6. TUNEL assay. A terminal deoxynucleotidyl transferase (TdT) dUTP Nick-End Labeling (TUNEL) assay was performed to determine the presence of apoptotic regions in the tumor tissue sections upon CuNPANP (1 and -5 mg kg^{-1}) treatment as per our published report[13] (for detailed procedure, see ESI†).

7.4.7. Western Blot analysis. The signaling pathways and molecular mechanisms involved in the melanoma inhibition potential of CuNPANP were investigated through Western blot analysis according to our published report.[13] The expression patterns of Bcl2, Bax, caspase 3, STAT3, GPX4, NRF2, SOD2, cytochrome c, cleaved caspase 3, p53, Akt, PI3K, mTOR and β-actin were investigated in both cell (B16F10) and tissue lysates (melanoma).

7.5. Statistical significance

Paired Student's *t*-test was used to evaluate all the experimental results, which were expressed as mean ± standard deviation (SD), and $^{**}p < 0.01$, $^{***}p < 0.001$ with respect to the control group were considered as statistically significant.

Data availability

The data that support the findings of this study will be made available upon request from the authors.

Author contributions

Sanchita Tripathy: design, overall planning *in vitro* and *in vivo* experiments, data analysis, manuscript preparation, Swapnali Londhe: contribution for *in vitro* and *in vivo* experiments, data analysis and participated in manuscript editing, Arti Patel: contribution for *in vitro* experiments, and participated in manuscript editing, Sudipta Saha: contribution for *in vitro* experiments, and participated in manuscript editing, Yogesh Chandra: significant contribution in histopathological analysis and participated in manuscript editing, Dr Chitta Ranjan Patra: conceived the original idea, design, overall planning, coordination, guidance and contribution for draft of the manuscript. Role as corresponding author.

Conflicts of interest

The authors declare that they have no known competing financial interests or personal relationships that could have appeared to influence the work reported in this paper.

Acknowledgements

This research is supported by DST, New Delhi under Core Research Grant under (CRG/2022/004594: GAP0985) and CSIR, New Delhi under PAN CSIR Cancer Research Program (HCP0040) to CRP. ST and SS are thankful to UGC for their Research Fellowship. SL is thankful to CSIR for her Research Fellowship. We thank Director, CSIR-IICT (Ms. No. IICT/Pubs./2024/136 dated April 16, 2024) for providing all the required facilities to carry out the work.

References

1 V. Monge-Fuentes, L. A. Muehlmann and R. B. de Azevedo, *Nano Rev.*, 2014, **5**, 24381.
2 V. Gray-Schopfer, C. Wellbrock and R. Marais, *Nature*, 2007, **445**, 851–857.
3 L. E. Davis, S. C. Shalin and A. J. Tackett, *Cancer Biol. Ther.*, 2019, **20**, 1366–1379.
4 Y. Liu and M. S. Sheikh, *Mol. Cell. Pharmacol.*, 2014, **6**, 228.
5 W. Guo, H. Wang and C. Li, *Signal Transduction Targeted Ther.*, 2021, **6**, 424.
6 N. H. Matthews, W.-Q. Li, A. A. Qureshi, M. A. Weinstock and E. Cho, *Epidemiology of Melanoma*, Exon Publications, 2017, pp. 3–22.
7 W. IARC, WHO Skin Cancer, **https://www.iarc.who.int/cancer-type/skin-cancer/#:~:text=Skin%20cancers%20are%20the%20most,people%20died%20from%20the%20disease**.
8 P. RESEARCH, 2023, **https://www.precedenceresearch.com/melanoma-therapeutics-market#:~:text=The%20global%20melanoma%20therapeutics%20market%20size%20is%20expected%20to%20increase,USD%205.5%20billion%20in%202022**.
9 A. C. Society, **https://www.cancer.org/cancer/types/melanoma-skin-cancer/about/key-statistics.html**.
10 N. C. Institute, 2023, **https://www.cancer.gov/types/skin/patient/melanoma-treatment-pdq**.
11 K. Li, G. Xiao, J. J. Richardson, B. L. Tardy, H. Ejima, W. Huang, J. Guo, X. Liao and B. Shi, *Adv. Sci.*, 2019, **6**, 1801688.
12 K. McNamara and S. A. Tofail, *Adv. Phys. X*, 2017, **2**, 54–88.
13 S. Tripathy, S. Haque, S. Londhe, S. Das, C. C. Norbert, Y. Chandra, B. Sreedhar and C. R. Patra, *Biomater. Adv.*, 2024, **160**, 213832.
14 S. Haque, R. Kotcherlakota, P. Bhamidipati, K. Muralidharan, B. Sreedhar, R. Amanchy and C. R. Patra, *Adv. Ther.*, 2023, **6**, 2300142.
15 S. Das, S. Tripathy, B. Sreedhar, S. Mukherjee and C. R. Patra, *Adv. Ther.*, 2023, **6**, 2200293.
16 S. Londhe, S. Haque, S. Tripathy, S. Bojja and C. R. Patra, *Nanoscale*, 2023, **15**, 10017–10032.
17 S. Tripathy, S. Londhe and C. R. Patra, *Biomed. Mater.*, 2024, **19**, 032001.
18 V. S. Madamsetty, M. K. Paul, A. Mukherjee and S. Mukherjee, *ACS Biomater. Sci. Eng.*, 2019, **6**, 167–181.
19 N. Chakraborty, J. Banerjee, P. Chakraborty, A. Banerjee, S. Chanda, K. Ray, K. Acharya and J. Sarkar, *Green Chem. Lett. Rev.*, 2022, **15**, 187–215.
20 K. Asif, M. Adeel, M. Mahbubur Rahman, M. Bartoletti, S. K. Brezar, M. Cemazar, V. Canzonieri, F. Rizzolio and I. Caligiuri, *Biomed. Pharmacother.*, 2024, **171**, 116017.

21 V. Oliveri, *Coord. Chem. Rev.*, 2020, **422**, 213474.
22 NIH, 2023, https://classic.clinicaltrials.gov/ct2/show/NCT03323346.
23 NIH, 2021, https://classic.clinicaltrials.gov/ct2/show/NCT02963051.
24 X. Kang, S. Jadhav, M. Annaji, C.-H. Huang, R. Amin, J. Shen, C. R. Ashby Jr, A. K. Tiwari, R. J. Babu and P. Chen, *Pharmaceutics*, 2023, **15**, 1567.
25 R. Mukhopadhyay, J. Kazi and M. C. Debnath, *Biomed. Pharmacother.*, 2018, **97**, 1373–1385.
26 R. Chakraborty and T. Basu, *Nanotechnology*, 2017, **28**, 105101.
27 Y. Wang, F. Yang, H. Zhang, X. Zi, X. Pan, F. Chen, W. Luo, J. Li, H. Zhu and Y. Hu, *Cell Death Dis.*, 2013, **4**, e783–e783.
28 D. Wang, H. Dong, M. Li, Y. Cao, F. Yang, K. Zhang, W. Dai, C. Wang and X. Zhang, *ACS Nano*, 2018, **12**, 5241–5252.
29 A. Djebli, A. Boudjemaa, H. Bendjeffal, H. Mamine, T. Metidji, H. Bekakria and Y. Bouhedja, *Inorg. Nano-Met. Chem.*, 2020, **50**, 1115–1122.
30 E. Musella, A. Mullaliu, T. Ruf, P. Huth, D. Tonelli, G. Aquilanti, R. Denecke and M. Giorgetti, *Energies*, 2020, **13**, 4027.
31 M. Ganiga and J. Cyriac, *ChemPhysChem*, 2016, **17**, 2315–2321.
32 M. Kumar, V. Bhatt, O. S. Nayal, S. Sharma, V. Kumar, M. S. Thakur, N. Kumar, R. Bal, B. Singh and U. Sharma, *Catal. Sci. Technol.*, 2017, **7**, 2857–2864.
33 D. Manzanares and V. Ceña, *Pharmaceutics*, 2020, **12**, 371.
34 M. Dolati, F. Tafvizi, M. Salehipour, T. Komeili Movahed and P. Jafari, *Sci. Rep.*, 2023, **13**, 3256.
35 V. Velma, S. R. Dasari and P. B. Tchounwou, *Biomarker Insights*, 2016, **11**, BMI. S39445.
36 N. Gong, X. Ma, X. Ye, Q. Zhou, X. Chen, X. Tan, S. Yao, S. Huo, T. Zhang and S. Chen, *Nat. Nanotechnol.*, 2019, **14**, 379–387.
37 D. R. Green and J. C. Reed, *science*, 1998, **281**, 1309–1312.
38 L. El Halal Schuch, M. M. Azevedo, R. Furian, P. Rigon, K. Cristine Reiter, I. Crivelatti, F. Riccardi and C. Giuliano Bica, *Appl. Cancer Res.*, 2019, **39**, 1–8.
39 X. Ma, Y. Wu, T. Zhang, H. Song, H. Jv, W. Guo and G. Ren, *J. Cancer*, 2017, **8**, 3828.
40 S. Silvestri, I. Porcellato, L. Mechelli, L. Menchetti, S. Iussich, R. De Maria, M. Sforna, L. Bongiovanni and C. Brachelente, *Vet. Pathol.*, 2020, **57**, 608–619.
41 X.-Z. Xu, M. V. Garcia, T.-y. Li, L.-Y. Khor, R. S. Gajapathy, C. Spittle, S. Weed, S. R. Lessin and H. Wu, *Mod. Pathol.*, 2010, **23**, 187–196.
42 V. Pautu, A. Mellinger, P. Resnier, E. Lepeltier, L. Martin, L. Boussemart, F. Letournel, C. Passirani and N. Clere, *J. Cancer Res. Clin. Oncol.*, 2019, **145**, 589–597.
43 J. C. Chamcheu, T. Roy, M. B. Uddin, S. Banang-Mbeumi, R.-C. N. Chamcheu, A. L. Walker, Y.-Y. Liu and S. Huang, *Cells*, 2019, **8**, 803.
44 A. Glaviano, A. S. Foo, H. Y. Lam, K. C. Yap, W. Jacot, R. H. Jones, H. Eng, M. G. Nair, P. Makvandi and B. Geoerger, *Mol. Cancer*, 2023, **22**, 138.
45 H.-H. Cao, D.-Y. Liu, Y.-C. Lai, Y.-Y. Chen, L.-Z. Yu, M. Shao and J.-S. Liu, *Front. Pharmacol.*, 2020, **11**, 748.
46 B. Perillo, M. Di Donato, A. Pezone, E. Di Zazzo, P. Giovannelli, G. Galasso, G. Castoria and A. Migliaccio, *Exp. Mol. Med.*, 2020, **52**, 192–203.
47 J. D. Hayes, A. T. Dinkova-Kostova and K. D. Tew, *Cancer Cell*, 2020, **38**, 167–197.
48 W. Chen, T. Jiang, H. Wang, S. Tao, A. Lau, D. Fang and D. D. Zhang, *Antioxid. Redox Signaling*, 2012, **17**, 1670–1675.
49 E. Obrador, F. Liu-Smith, R. W. Dellinger, R. Salvador, F. L. Meyskens and J. M. Estrela, *Biol. Chem.*, 2019, **400**, 589–612.
50 M. Gagliardi, D. Cotella, C. Santoro, D. Corà, N. A. Barlev, M. Piacentini and M. Corazzari, *Cell Death Dis.*, 2019, **10**, 902.
51 K. Khorsandi, H. Esfahani, S.-K. Ghamsari and P. Lakhshehei, *Cell Commun. Signaling*, 2023, **21**, 337.
52 M. J. Kerins and A. Ooi, *Antioxid. Redox Signaling*, 2018, **29**, 1756–1773.
53 T. Sinnberg, K. Lasithiotakis, H. Niessner, B. Schittek, K. T. Flaherty, D. Kulms, E. Maczey, M. Campos, J. Gogel, C. Garbe and F. Meier, *J. Invest. Dermatol.*, 2009, **129**, 1500–1515.
54 E. Panieri and M. Santoro, *Cell Death Dis.*, 2016, **7**, e2253–e2253.
55 S. Mukherjee, R. Kotcherlakota, S. Haque, S. Das, S. Nuthi, D. Bhattacharya, K. Madhusudana, S. Chakravarty, R. Sistla and C. R. Patra, *ACS Biomater. Sci. Eng.*, 2020, **6**, 690–704.
56 E. Obrador, S. L. Valles, M. Benlloch, J. A. Sirerol, J. A. Pellicer, J. Alcacer, J. A.-F. Coronado and J. M. Estrela, *PLoS One*, 2014, **9**, e96466.
57 J. Q. Tang, X. Y. Hou, C. S. Yang, Y. X. Li, Y. Xin, W. W. Guo, Z. P. Wei, Y. Q. Liu and G. Jiang, *Int. J. Cancer*, 2017, **141**, 646–653.
58 L. Zeng, B. J. Gowda, M. G. Ahmed, M. A. Abourehab, Z.-S. Chen, C. Zhang, J. Li and P. Kesharwani, *Mol. Cancer*, 2023, **22**, 10.
59 K. Asif, M. Adeel, M. M. Rahman, I. Caligiuri, T. Perin, M. Cemazar, V. Canzonieri and F. Rizzolio, *J. Mater. Chem. B*, 2023, **11**, 3124–3135.
60 M. Griffiths and H. Sundaram, *Cancer Cell Culture: Methods and Protocols*, 2011, pp. 451–465.
61 N. Mundhara, A. Majumder and D. Panda, *Sci. Rep.*, 2019, **9**, 7638.